Article

Not peer-reviewed version

Spatiotemporal Modelling of CAR-T Cell Therapy in Solid Tumours: Mechanisms of Antigen Escape and Immunosuppression

Maxim Polyakov *

Posted Date: 11 March 2026

doi: 10.20944/preprints202603.0742.v1

Keywords: mathematical modelling; computational oncology; CAR-T therapy; computational algorithms; reaction–diffusion system; partial differential equations; antigen heterogeneity; tumour microenvironment; spatiotemporal dynamics

 doi:10.20944/preprints202603.0742.v1

Article

Spatiotemporal Modelling of CAR-T Cell Therapy in Solid Tumours: Mechanisms of Antigen Escape and Immunosuppression

Maxim Polyakov

Department of Information Systems and Computer Modelling, Volgograd State University, Universitetsky pr., 100, Volgograd 400062, Russia; m.v.polyakov@volsu.ru

Abstract

Although chimeric antigen receptor T-cell therapy (CAR-T) has shown substantial efficacy in haematological malignancies, its application to solid tumours remains limited by antigenic heterogeneity, poor effector-cell infiltration, and an immunosuppressive tumour microenvironment. This study aimed to develop a mathematical model of the spatiotemporal dynamics of a solid tumour under CAR-T cell therapy, incorporating the main determinants of therapeutic resistance. We propose a reaction–diffusion model formulated as a system of partial differential equations describing functional and exhausted CAR-T cells, antigen-positive and antigen-negative tumour subpopulations, and chemokine, immunosuppressive, and hypoxic fields. The model was analysed using steady-state analysis and numerical simulations based on a finite-difference scheme. The simulations showed that therapeutic outcome is governed by the combined effects of CAR-T cell infiltration, functional exhaustion, and tumour antigen escape. The model reproduced partial tumour regression followed by persistence of a residual tumour population, the emergence of an antigen-negative component under therapeutic pressure, and reduced treatment efficacy under more strongly immunosuppressive and hypoxic microenvironmental conditions. Repeated simulated CAR-T-cell administration improved tumour control, albeit with diminishing returns. Overall, the proposed model provides a useful framework for analysing resistance mechanisms and optimising CAR-T cell therapy protocols for solid tumours.

Keywords: mathematical modelling; computational oncology; CAR-T therapy; computational algorithms; reaction–diffusion system; partial differential equations; antigen heterogeneity; tumour microenvironment; spatiotemporal dynamics

1. Introduction

Cancer immunotherapy, particularly chimeric antigen receptor T-cell (CAR-T) therapy, is one of the most important advances in modern oncology. Its clinical potential has been demonstrated in haematological malignancies, where high rates of complete remission have been reported in patients with relapsed or refractory disease [1,2]. However, despite these remarkable advances in haematology, the efficacy of CAR-T therapy against solid tumours remains limited [3,4]. Solid tumours orchestrate a complex network of physical, biological, and immunological barriers that collectively impede the infiltration, persistence, and function of CAR-T cells [5,6].

The application of CAR-T therapy to solid tumours is limited by several major challenges, including heterogeneity of tumour antigen expression, restricted penetration of CAR-T cells into the tumour mass, an immunosuppressive tumour microenvironment, and T-cell exhaustion [7,8]. Antigenic heterogeneity is particularly important because antigen-positive and antigen-negative cells can coexist within a single tumour, creating selective pressure and promoting immune escape [9]. Mathematical models that incorporate this mechanism may help to investigate treatment dynamics

 doi:10.20944/preprints202603.0742.v1

and predict the emergence of resistance [10]. Another important aspect is the bystander effect, whereby CAR-T cells can activate endogenous antitumour T lymphocytes directed against antigens not directly recognised by the CAR [9]. Understanding and quantitatively characterising these complex processes requires the application of modern mathematical and computational modelling approaches. For clarity, the principal limitations of CAR-T therapy in solid tumours, together with the corresponding directions of mathematical modelling, are shown in Figure 1. The following section briefly reviews the main classes of models used to describe tumour growth and tumour–immune interactions.

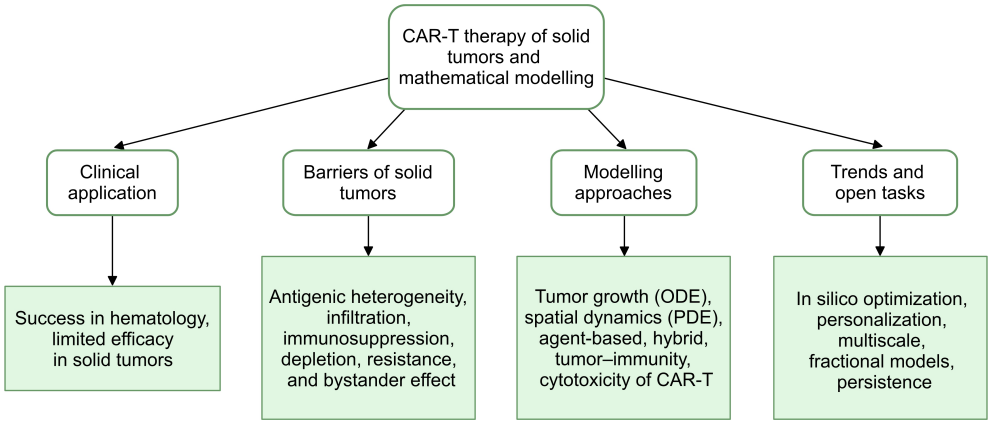

Figure 1. Key barriers to the efficacy of CAR-T cell therapy in solid tumours and the corresponding directions of mathematical modelling.

Mathematical modelling of biological processes has been widely employed in oncology research over recent decades [11,12]. Mathematical, physical, and computational approaches have been widely used to investigate various aspects of tumour growth and to improve our understanding of tumour responses to clinical interventions [13,14]. In silico studies that predict individual patient responses to different dosing schedules or combinations of treatment modalities are becoming an invaluable tool for optimising medical therapy [15]. Numerous mathematical models have been developed to describe tumour growth dynamics. These models may be classified according to various criteria, including spatial scale (subcellular, cellular, tissue, and organismal), the type of mathematical formalism employed (ordinary differential equations, partial differential equations, agent-based models, and hybrid approaches), and the biological processes considered (proliferation, apoptosis, angiogenesis, and interactions with the immune system) [16,17]. Classic tumour growth models, such as exponential, logistic, and Gompertz models, are widely used to describe tumour growth kinetics [18,19]. More sophisticated approaches account for the spatial heterogeneity of the tumour and its microenvironment by using diffusion equations and methods from elasticity theory [20,21]. Of particular interest are hybrid models that combine both discrete and continuous variables to represent individual cells and concentration or density fields, respectively [17]. Each discrete cell may be equipped with submodels that govern cellular behaviour in response to microenvironmental signals. Moreover, individual cells interact with one another and collectively form an integrated tissue. Hybrid models constitute a broader class of individual-based models that are closely aligned with tumour cell biology and allow the incorporation of multiple interacting intracellular and extracellular variables. They are therefore particularly well suited to systems biology approaches to the study of tumour growth [22].

In recent years, increasing attention has been directed towards modelling interactions between tumours and the immune system [23,24]. These models describe the complex dynamics between tumour cells and various components of the immune system, including T lymphocytes, natural killer cells, macrophages, and dendritic cells [25,26]. Models of tumour–immune system interactions allow us to investigate the conditions under which the immune system is able to control tumour growth and to predict the effectiveness of various immunotherapeutic strategies [27,28]. With the advent of CAR-T cell therapy, there has been a growing need for specialised mathematical models capable of adequately capturing the distinctive features of this treatment modality [29,30]. Unlike conventional

 doi:10.20944/preprints202603.0742.v1

chemotherapy, which exhibits predictable dose–exposure relationships, the dynamics of CAR-T cells depend on complex biological factors that determine treatment response [31]. Contemporary models of CAR-T cell therapy may be divided into several categories: pharmacokinetic models describing the expansion and persistence of CAR-T cells in the body, models of cellular cytotoxicity describing the elimination of tumour cells by CAR-T cells, and more comprehensive models that account for the spatial organisation of the tumour and its microenvironment [32,33].

Particularly challenging is the modelling of the spatiotemporal dynamics of solid tumours under CAR-T cell therapy. Spatial aspects play a crucial role in therapeutic efficacy, as CAR-T cell distribution within the tumour, nutrient availability, oxygen gradients, and spatial heterogeneity of antigen expression significantly influence treatment outcomes [34,35]. Tumour geometry may also exert a marked effect on treatment efficacy in silico, with notable differences observed between tumours with block-like architectures and those with sparse cellular distributions, giving rise to the concept of immunosuppression driven by geometric effects [34]. Another important direction is the development of models that account for mechanisms of resistance to CAR-T cell therapy [36]. Long-term studies of CAR-T cell therapy have revealed that remissions are often not durable in a substantial proportion of patients. Among the mechanisms underlying these relapses are limited cytotoxicity or persistence of CAR-T cells, as well as antigen loss or lineage switching in tumour cells [36]. Mathematical models that use a continuous variable to describe the level of antigen expression in tumour cells make it possible to reproduce key cellular mechanisms in patients exhibiting different therapeutic responses [36].

Contemporary approaches to the mathematical modelling of tumour growth increasingly integrate methods from artificial intelligence and big-data analytics [15]. This includes, in particular, the use of machine learning to calibrate and adapt mathematical models to individual patient data [37]. Personalised mechanistic models combined with machine-learning methods open new possibilities for predicting therapeutic response and optimising treatment for each individual patient [15,38]. However, a fundamental barrier to the implementation of this paradigm is the current lack of a rigorous yet practical mathematical theory of tumour initiation, progression, invasion, and therapeutic response [15]. In the context of modelling CAR-T cell therapy for solid tumours, multiscale approaches are of particular relevance, as they account for processes across different levels of biological organisation, from intracellular signalling pathways to the tissue architecture of the tumour and the systemic immune response of the host [39,40]. Such models make it possible to investigate complex non-linear interactions between system components and to identify critical points at which small parameter changes may substantially affect treatment outcome [41]. Another promising direction is the use of fractional calculus and fractional differential equations to model tumour dynamics [18,42]. Fractional models may provide a better description of complex processes with memory and non-local interactions, which are characteristic of biological systems. Studies indicate that fractional models can offer greater accuracy and stability than classical integer-order models [42].

Despite substantial progress in the mathematical modelling of CAR-T cell therapy, a number of unresolved challenges remain. These include an adequate description of the spatiotemporal dynamics of CAR-T cell infiltration into solid tumours, taking into account the influence of tumour microenvironment heterogeneity on CAR-T cell function, predicting the long-term persistence of CAR-T cells, and developing models for optimising combination therapies [43,44].

In this article, we present a comprehensive mathematical model of the spatiotemporal dynamics of solid tumours under CAR-T cell therapy. The model integrates key aspects of tumour growth, immune response, and treatment, including antigenic heterogeneity, spatial cell distribution, and mechanisms of cytotoxicity and immunosuppression. Unlike existing approaches, which usually focus on only some of these processes, the model brings them together within a single reaction–diffusion–chemotaxis framework. This framework allows the simultaneous analysis of CAR-T-cell migration through heterogeneous tissue, functional exhaustion and partial recovery, dynamic switching between antigen-positive and antigen-low tumour phenotypes under therapeutic pressure, and the effects of chemoattractant, soluble immunosuppressive factors, and hypoxia. The model therefore captures not only the selection

 doi:10.20944/preprints202603.0742.v1

of pre-existing tumour subclones but also adaptive antigen escape, providing a more realistic basis for studying the spatially dependent response of solid tumours to CAR-T cell therapy.

This study aimed to develop and analyse a spatiotemporal mathematical model of the interaction between CAR-T cells and solid tumours. The model incorporates antigenic heterogeneity, spatial distribution of cellular populations, and mechanisms of cytotoxicity, functional exhaustion, and immunosuppression, with the aim of identifying the key factors governing CAR-T cell infiltration, therapeutic efficacy, and tumour escape.

This work is organised as follows. Section 2 presents the problem formulation and computational methods. Subsection 2.1 introduces the spatiotemporal model of the interaction between CAR-T cells and a solid tumour. Subsection 2.2 examines the steady states and local stability of the spatially homogeneous version of the model, and Subsection 2.3 describes the numerical methods and software implementation. Section 3 presents the results of the computational experiments. Subsection 3.1 examines the typical dynamics of the spatially homogeneous system under baseline parameter values. Subsection 3.2 considers the baseline scenario of CAR-T cell infiltration and tumour elimination in the absence of antigenic heterogeneity. Subsection 3.3 analyses the effects of antigenic heterogeneity and phenotypic switching on therapeutic outcome, and Subsection 3.4 investigates the role of the immunosuppressive factor and hypoxia in determining CAR-T cell efficacy. Section 4 discusses the biological interpretation of the results, the limitations of the model, and possible directions for further development, and Section 5 summarises the main conclusions.

2. Materials and Methods

2.1. Spatiotemporal Mathematical Model of the Interaction Between CAR-T Cells and a Solid Tumour

To model the spatiotemporal interactions between CAR-T cells and a solid tumour while accounting for the principal biological constraints, we propose a coupled system of non-linear partial differential equations. We consider the following unknown functions, each depending on the spatial variable $\mathbf{x} = (x, y, z) \in \mathbb{R}^3$ and time t. Here, $C(\mathbf{x}, t)$ denotes the density of functional CAR-T cells, $E(\mathbf{x}, t)$ the density of exhausted CAR-T cells, and $T_A(\mathbf{x}, t)$ and $T_B(\mathbf{x}, t)$ the densities of tumour cells expressing the target antigen and of tumour cells with low antigen expression, respectively. Furthermore, $S(\mathbf{x}, t)$ denotes the concentration of the chemoattractant, $A(\mathbf{x}, t)$ the concentration of a generalised soluble immunosuppressive factor, such as transforming growth factor-β (TGF-β), interleukin-10 (IL-10), or adenosine, and $H(\mathbf{x}, t)$ the normalised level of hypoxia in the microenvironment. The dynamics of these quantities are described by the following system of reaction–diffusion–chemotaxis equations

$$
\begin{cases}
\dfrac{\partial C}{\partial t} = \nabla\cdot\big(D_C(\mathbf{x})\nabla C\big) - \nabla\cdot\big(\chi_C(A)\, C\, \nabla S\big) + \rho_C \dfrac{C\, T_A}{K_C + C} \\
\qquad\qquad - \delta_{CT}\, C\, T_A - k_e(A, H)\, C + \dfrac{p_r}{1 + A}\, E - d_C\, C, & (1) \\
\dfrac{\partial E}{\partial t} = \nabla\cdot\big(D_E \nabla E\big) + k_e(A, H)\, C - \dfrac{p_r}{1 + A}\, E - d_E\, E, & (2) \\
\dfrac{\partial T_A}{\partial t} = \nabla\cdot\big(D_T \nabla T_A\big) + r_T\left(1 - \dfrac{T_A + T_B}{K_T}\right) T_A - \gamma\, C\, T_A \\
\qquad\qquad - \mu_{AB}(C)\, T_A + \mu_{BA}(C)\, T_B - d_{T_A}\, T_A, & (3) \\
\dfrac{\partial T_B}{\partial t} = \nabla\cdot\big(D_T \nabla T_B\big) + r_T\left(1 - \dfrac{T_A + T_B}{K_T}\right) T_B + \mu_{AB}(C)\, T_A \\
\qquad\qquad - \mu_{BA}(C)\, T_B - d_{T_B}\, T_B, & (4) \\
\dfrac{\partial S}{\partial t} = D_S\, \nabla^2 S + \sigma_S\, T_A - \lambda_S\, S, & (5) \\
\dfrac{\partial A}{\partial t} = D_A\, \nabla^2 A + \sigma_A\, (T_A + T_B) + \sigma_M\, f(H) - \lambda_A\, A, & (6) \\
\dfrac{\partial H}{\partial t} = D_H\, \nabla^2 H + \eta\, (T_A + T_B) - \lambda_H\, H. & (7)
\end{cases}
$$

 doi:10.20944/preprints202603.0742.v1

The coefficients $\chi_C(A)$, $k_e(A,H)$, $\mu_{AB}(C)$, and $\mu_{BA}(C)$, together with the function $f(H)$, describe how chemotaxis, the exhaustion rate, and phenotypic transition rates depend on the microenvironment

$$\begin{aligned} &\chi_C(A) = \frac{\chi_0}{1+\alpha_A\,A}, \quad k_e(A,H) = k_e^0\,(1+\beta_A\,A+\beta_H\,H), \quad \mu_{AB}(C) = \mu_0 + \nu\,C, \\ &\mu_{BA}(C) = \mu_1\,\exp(-\xi\,C), \quad f(H) = \frac{H}{K_H+H}. \end{aligned} \tag{8}$$

A schematic representation of the key interactions between the cellular populations and the microenvironmental factors in the spatiotemporal model is shown in Figure 2. The first pair of equations, (1)–(2), describes the dynamics of adoptively transferred CAR-T cells. These equations combine passive diffusive migration $\nabla\cdot(D_C(\mathbf{x})\nabla C)$, which accounts for anatomical barriers within the tissue through the spatially dependent coefficient $D_C(\mathbf{x})$, and chemotaxis along the gradient of the chemoattractant S, given by the term $-\nabla\cdot(\chi_C(A)\,C\,\nabla S)$ and modulated by the level of immunosuppression via $\chi_C(A)$ in accordance with the classical Keller–Segel model [45]. Saturable proliferation of CAR-T cells, induced by activation upon contact with antigen-positive tumour cells, is modelled by the term $\rho_C\,\frac{C\,T_A}{K_C+C}$, whereas their cytotoxic activity is described by the linear term $-\delta_{CT}\,C\,T_A$. Since both processes depend on the product $C\,T_A$, the parameters ρ_C and δ_{CT} require separate experimental calibration. The microenvironment promotes exhaustion of effector cells through the rate $k_e(A,H)$, which increases with increasing concentration of the immunosuppressive factor A and the degree of hypoxia H, whereas reversible transitions to a dysfunctional state and recovery are accounted for by the term $\frac{p_r}{1+A}\,E$. The terms $d_C\,C$ and $d_E\,E$ describe the natural death of CAR-T cells.

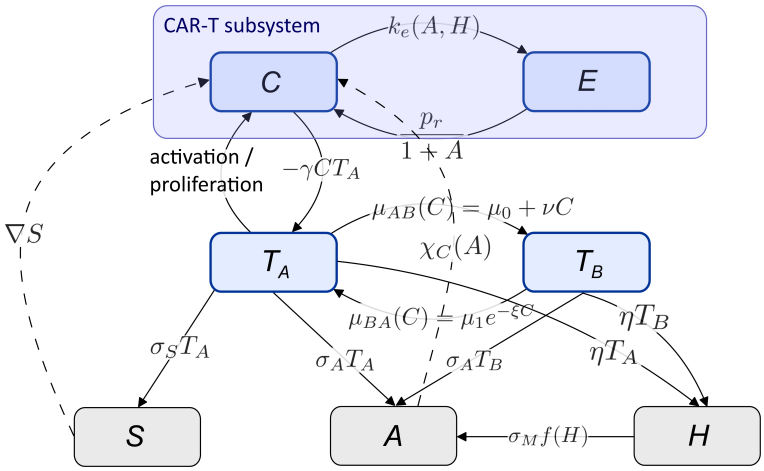

Figure 2. Schematic representation of the key interactions in the spatiotemporal model of CAR-T cell therapy for solid tumours. The principal cause-and-effect relationships between the cellular populations and the fields of the tumour microenvironment are shown.

Equations (3)–(4) characterise the dynamics of the two phenotypic subpopulations of tumour cells. Their growth follows a logistic law with a shared carrying capacity K_T. CAR-T cells eliminate only the antigen-positive cells T_A at rate γ. The key mechanism of antigen escape is formalised through phenotypic switching. The rate of antigen loss $\mu_{AB}(C)$ increases linearly with the concentration of CAR-T cells, reflecting selective pressure and therapy-induced loss of expression, whereas the reverse transition $\mu_{BA}(C)$ is exponentially suppressed in the presence of CAR-T cells, corresponding to the cessation of antigen expression as a protective response. This formulation allows us to describe the dynamic adaptation of the tumour, rather than merely the selection of pre-existing clones. In both equations, the logistic term $r_T(1-\frac{T_A+T_B}{K_T})\,T_{A,B}$ determines the proliferation rate, whereas the terms $d_{T_A}\,T_A$ and $d_{T_B}\,T_B$ define natural cell death.

The last three equations (5)–(7) describe the evolution of the biochemical fields. The chemoattractant S diffuses and is produced by antigen-positive cells T_A at the rate σ_S, thereby providing the signal for the directed migration of CAR-T cells, and degrades with coefficient λ_S. The generalised

 doi:10.20944/preprints202603.0742.v1

immunosuppressive factor A is produced by both tumour subpopulations at the rate σ_A and is further enhanced by hypoxia through $\sigma_M f(H)$, reflecting the increased secretion of cytokines and metabolites in regions deficient in oxygen. It also diffuses and decays with coefficient λ_A. The variable H represents the degree of hypoxia, which increases in proportion to the total density of tumour cells with coefficient η and decreases due to perfusion and buffering processes with coefficient λ_H. The system is supplemented by initial conditions for all variables at $t = 0$ and by Neumann boundary conditions at the boundary $\partial\Omega$, corresponding to an isolated modelled tissue volume.

The initial parameter values used in the numerical experiments are listed in Table 1 along with their acceptable ranges. These parameters determine spatial transport, cell kinetics, and microenvironment dynamics. Most of them were based on published experimental estimates (see Table 1), while parameters for which no direct measurements were available were assigned physiologically plausible ranges, which were subsequently verified using sensitivity analysis and model calibration. These ranges define the initial parameter space and allow us to assess the robustness of qualitative conclusions to parameter uncertainty.

Table 1. Initial values of the free model parameters.

Parameter	Description	Value in the model	Range of values
D_C	Diffusion coefficient of functional CAR-T cells	0.014	0.014 cm^2/day [46]
D_T	Diffusion coefficient of tumour cells	5×10^{-5}	10^{-5}–10^{-4} cm^2/day [46]
D_E	Diffusion coefficient of exhausted CAR-T cells	0.001	0.0006–0.0014 cm^2/day [47,48]
D_S	Diffusion coefficient of chemokine S	0.0045	0.00086–0.0086 cm^2/day [49]
D_A	Diffusion coefficient of immunosuppressive factor A (cytokine such as IL-6/IL-10)	0.02	(0.007–0.086) cm^2/day [50]
D_H	Diffusion coefficient of hypoxia variable (oxygen)	1.5	0.86–1.8 cm^2/day [51,52]
ρ_C	Proliferation rate of CAR-T cells	0.55	0.1–0.9 day^{-1} [53]
r_T	Tumour growth rate	0.13	0.01–0.25 day^{-1} [46,53]
δ_{CT}	Rate of tumour-cell killing by CAR-T cells	0.41	0.3–0.6 day^{-1} [9]
d_C	Death rate of functional CAR-T cells	0.08	0.03–0.14 day^{-1} [9,53]
k_e^0	Baseline exhaustion rate of CAR-T cells	0.05	0.03–0.07 day^{-1} [53]
K_C	Half-saturation constant for CAR-T proliferation	2×10^9	10^8–10^{10} cells [53]
K_T	Carrying capacity of tumour cells	2.4×10^8	(1–5) $\times 10^8$ cells cm^{-3} [46]
σ_S	Production rate of chemokine S	5×10^{-4}	(1–10) $\times 10^{-4}$ mg ml^{-1} day^{-1} [54]
λ_S	Decay rate of chemokine S	0.56	0.4–0.8 day^{-1} [55]
σ_A	Production rate of immunosuppressive factor A	5×10^{-3}	(1–10) $\times 10^{-3}$ mg ml^{-1} day^{-1} [56]
σ_M	Additional production rate of A induced by hypoxia	0.002	0.001–0.005 mg ml^{-1} day^{-1} [56]
λ_A	Decay rate of immunosuppressive factor A	0.75	0.5–1.5 day^{-1} [55]
η	Rate of hypoxia accumulation per tumour cell	5×10^{-10}	10^{-10}–10^{-9} day^{-1} $cell^{-1}$ [53]
λ_H	Decay rate of hypoxia	0.43	0.17–0.69 day^{-1} [57]
χ_0	Chemotactic sensitivity coefficient	0.1	assumed
p_r	Recovery rate from T-cell exhaustion	0.1	0.07–0.14 day^{-1} [58]
d_E	Death rate of exhausted CAR-T cells	0.04	0.02–0.05 day^{-1} [59]
d_{T_A}	Natural death rate of antigen-positive tumour cells	0.01	0.005–0.02 day^{-1} [60]
d_{T_B}	Natural death rate of antigen-negative tumour cells	0.01	0.005–0.02 day^{-1} [60]
μ_0	Baseline rate of antigen loss ($T_A \to T_B$ switching)	0.13	0.11–0.16 day^{-1} [61]
μ_1	Baseline rate of antigen recovery ($T_B \to T_A$ switching)	0.07	0.057–0.089 day^{-1} [61]
ν	Effect of CAR-T cell density on antigen loss	1×10^{-10}	assumed
ξ	CAR-T–dependent suppression of antigen recovery	1×10^{-9}	assumed
α_A	Suppression of chemotaxis by immunosuppressive factor	1.0	assumed
β_A	Increase in exhaustion rate per unit of A	1.0	assumed
β_H	Increase in exhaustion rate per unit of hypoxia	1.0	assumed
K_H	Half-saturation constant for hypoxia effect in $f(H)$	0.5	assumed

 doi:10.20944/preprints202603.0742.v1

2.2. Steady States and Local Stability of the Spatially Homogeneous Version of the Model

In this subsection, we analytically investigate the steady states and their local stability for the spatially homogeneous version of model (1)–(7). To this end, we consider spatially homogeneous solutions of the form

$$C(\mathbf{x},t) = C(t), \quad E(\mathbf{x},t) = E(t), \quad T_A(\mathbf{x},t) = T_A(t), \quad T_B(\mathbf{x},t) = T_B(t),$$

$$S(\mathbf{x},t) = S(t), \quad A(\mathbf{x},t) = A(t), \quad H(\mathbf{x},t) = H(t),$$

for which the spatial derivatives and the diffusion, and chemotactic fluxes vanish

$$\nabla u \equiv 0, \quad \nabla^2 u \equiv 0, \quad \nabla \cdot (\chi_C C \nabla S) \equiv 0.$$

As a result, system (1)–(7) reduces to a system of ordinary differential equations of the form

$$\begin{cases} \dot{C} = \rho_C \dfrac{C\,T_A}{K_C + C} - \delta_{CT}\, C\, T_A - k_e(A,H)\, C + \dfrac{p_r}{1+A}\, E - d_C\, C, & (9)\\ \dot{E} = k_e(A,H)\, C - \dfrac{p_r}{1+A}\, E - d_E\, E, & (10)\\ \dot{T}_A = r_T\left(1 - \dfrac{T_A + T_B}{K_T}\right) T_A - \gamma\, C\, T_A - \mu_{AB}(C)\, T_A + \mu_{BA}(C)\, T_B - d_{T_A}\, T_A, & (11)\\ \dot{T}_B = r_T\left(1 - \dfrac{T_A + T_B}{K_T}\right) T_B + \mu_{AB}(C)\, T_A - \mu_{BA}(C)\, T_B - d_{T_B}\, T_B, & (12)\\ \dot{S} = \sigma_S\, T_A - \lambda_S\, S, & (13)\\ \dot{A} = \sigma_A\,(T_A + T_B) + \sigma_M\, f(H) - \lambda_A\, A, & (14)\\ \dot{H} = \eta\,(T_A + T_B) - \lambda_H\, H. & (15) \end{cases}$$

where the auxiliary functions are defined by relations

$$\chi_C(A) = \frac{\chi_0}{1 + \alpha_A A}, \qquad k_e(A,H) = k_e^0\,(1 + \beta_A A + \beta_H H), \tag{16}$$

$$\mu_{AB}(C) = \mu_0 + \nu C, \qquad \mu_{BA}(C) = \mu_1\, \exp(-\xi C), \qquad f(H) = \frac{H}{K_H + H}. \tag{17}$$

The steady state of system (9)–(15) is defined by the condition

$$\dot{C} = \dot{E} = \dot{T}_A = \dot{T}_B = \dot{S} = \dot{A} = \dot{H} = 0.$$

We next consider three biologically relevant classes of steady states:

- a completely healthy state in the absence of both tumour cells and CAR-T cells,
- a tumour state in the absence of CAR-T cells,
- a coexistence state involving both the tumour and CAR-T cells.

The completely healthy steady state corresponds to the absence of a tumour, that is

$$T_A^* = 0, \qquad T_B^* = 0.$$

From (13)–(15), it then follows that

$$S^* = 0, \qquad A^* = 0, \qquad H^* = 0.$$

 doi:10.20944/preprints202603.0742.v1

Substitution into (9) and (10) yields a linear system for (C^*, E^*):

$$0 = -(k_e^0 + d_C)\, C^* + p_r E^*, \tag{18}$$
$$0 = k_e^0 C^* - (p_r + d_E)\, E^*. \tag{19}$$

For positive parameter values, the unique non-negative solution to (18)–(19) is given by

$$C^* = 0, \qquad E^* = 0.$$

Thus, the completely healthy steady state is given by

$$E_0 : \qquad (C^*, E^*, T_A^*, T_B^*, S^*, A^*, H^*) = (0,0,0,0,0,0,0). \tag{20}$$

The tumour state in the absence of CAR-T cells is described by the steady state

$$C^* = 0, \qquad E^* = 0, \qquad T_A^* \geq 0, \qquad T_B^* \geq 0,$$

with a non-zero tumour burden. At $C^* = 0$, (17) yields

$$\mu_{AB}(0) = \mu_0, \qquad \mu_{BA}(0) = \mu_1.$$

Then, from the equations for the soluble factors (13)–(15), we obtain

$$S^* = \frac{\sigma_S}{\lambda_S} T_A^*, \tag{21}$$
$$H^* = \frac{\eta}{\lambda_H}\,(T_A^* + T_B^*) = \frac{\eta}{\lambda_H} N^*, \quad N^* = T_A^* + T_B^*, \tag{22}$$
$$A^* = \frac{1}{\lambda_A}\Big[\sigma_A N^* + \sigma_M f(H^*)\Big]. \tag{23}$$

The steady-state equations for the tumour populations (11) and (12) at $C^* = 0$ take the form

$$0 = r_T\Big(1 - \frac{N^*}{K_T}\Big) T_A^* - d_{T_A} T_A^* - \mu_0 T_A^* + \mu_1 T_B^*, \tag{24}$$
$$0 = r_T\Big(1 - \frac{N^*}{K_T}\Big) T_B^* - d_{T_B} T_B^* + \mu_0 T_A^* - \mu_1 T_B^*. \tag{25}$$

System (24)–(25) is non-linear with respect to the variables T_A^*, T_B^*, since the coefficient

$$R(N^*) = r_T\Big(1 - \frac{N^*}{K_T}\Big)$$

depends on their sum N^*. For its analysis, it is convenient to add the two equations, which yields the following condition for the total tumour burden N^*

$$\Big[r_T\Big(1 - \frac{N^*}{K_T}\Big)\Big] N^* = d_{T_A} T_A^* + d_{T_B} T_B^*. \tag{26}$$

We consider two biologically relevant cases. The first corresponds to an antigenically homogeneous tumour, that is, the pre-treatment setting. If, before the initiation of therapy, the tumour consists solely of antigen-positive cells, then

$$T_B^* = 0, \qquad N^* = T_A^*.$$

 doi:10.20944/preprints202603.0742.v1

Then, from (24), we obtain the equation for T_A^*

$$0 = r_T\Big(1 - \frac{T_A^*}{K_T}\Big)T_A^* - (d_{T_A} + \mu_0)T_A^*.$$

A non-zero solution exists for $r_T > d_{T_A} + \mu_0$ and is given by

$$T_A^* = K_T\Big(1 - \frac{d_{T_A} + \mu_0}{r_T}\Big), \quad T_B^* = 0. \tag{27}$$

If $T_A^*, T_B^* > 0$, then equations (24) and (25) can be rewritten as a homogeneous linear system with respect to T_A^*, T_B^* for fixed N^*

$$\begin{pmatrix} R(N^*) - d_{T_A} - \mu_0 & \mu_1 \\ \mu_0 & R(N^*) - d_{T_B} - \mu_1 \end{pmatrix}\begin{pmatrix} T_A^* \\ T_B^* \end{pmatrix} = \begin{pmatrix} 0 \\ 0 \end{pmatrix}.$$

For a non-trivial solution to exist, the determinant of the matrix must vanish

$$\big[R(N^*) - d_{T_A} - \mu_0\big]\big[R(N^*) - d_{T_B} - \mu_1\big] - \mu_0\mu_1 = 0. \tag{28}$$

Expanding the brackets yields a quadratic equation for $R(N^*)$

$$\big[R(N^*)\big]^2 - \big(d_{T_A} + d_{T_B} + \mu_0 + \mu_1\big)R(N^*) + \big(d_{T_A} + \mu_0\big)\big(d_{T_B} + \mu_1\big) - \mu_0\mu_1 = 0.$$

Its discriminant

$$\Delta = \big(d_{T_A} + d_{T_B} + \mu_0 + \mu_1\big)^2 - 4\Big[\big(d_{T_A} + \mu_0\big)\big(d_{T_B} + \mu_1\big) - \mu_0\mu_1\Big]$$

is non-negative for typical parameter values. Each positive root, R_1 or R_2, yields a corresponding value of the total tumour burden through inversion of the relation $R(N^*) = r_T(1 - \frac{N^*}{K_T})$

$$N_k^* = K_T\Big(1 - \frac{R_k}{r_T}\Big), \quad k = 1, 2. \tag{29}$$

For each admissible $N_k^* > 0$, the population ratio is obtained from either of equations (24)–(25)

$$\frac{T_B^*}{T_A^*} = \frac{d_{T_A} + \mu_0 - R(N^*)}{\mu_1} = \frac{\mu_0}{R(N^*) - d_{T_B} - \mu_1}. \tag{30}$$

A biologically realistic steady state must satisfy the conditions $T_A^*, T_B^*, N^* > 0$ and $N^* < K_T$. In the subsequent analysis, we assume that, in the absence of therapy, the tumour is in one of these steady states, denoted by

$$E_T: \quad C^* = E^* = 0, \quad T_A^*, T_B^* > 0, \quad S^*,\ A^*,\ H^* \text{ are defined by the equations (21)–(23).} \tag{31}$$

In this work, primary attention is devoted to the case of a homogeneous antigen-positive tumour, as this is the most relevant setting at the initiation of CAR-T therapy. The existence of a mixed steady state indicates the fundamental possibility of tumour persistence through a dynamic balance between phenotypes even in the absence of immune pressure.

The coexistence state of the tumour and CAR-T cells corresponds to steady state

$$E_{CT}: \quad C^* > 0, \quad E^* \geq 0, \quad T_A^* > 0, \quad T_B^* \geq 0,$$

which satisfies the full system of steady-state equations (9)–(15). It is not possible to express $(C^*, E^*, T_A^*, T_B^*, S^*, A^*, H^*)$ explicitly, and their values are therefore most appropriately determined

 doi:10.20944/preprints202603.0742.v1

numerically. In what follows, we use the notation E_{CT} for such a steady state and analyse its local stability on the basis of the Jacobian of the system.

To investigate linear stability, we introduce the vector of variables

$$\mathbf{u} = (C, E, T_A, T_B, S, A, H)^\top,$$

and denote the right-hand sides of system (9)–(15) by $\dot{\mathbf{u}} = F(\mathbf{u})$. The Jacobian takes the form

$$J(\mathbf{u}) = \frac{\partial F}{\partial \mathbf{u}}(\mathbf{u}).$$

The structure of system (9)–(15) is such that the subsystem (S, A, H) is linear in these variables and is governed by the equations

$$\dot{S} = \sigma_S T_A - \lambda_S S, \quad \dot{A} = \cdots - \lambda_A A, \quad \dot{H} = \cdots - \lambda_H H.$$

Therefore, the eigenvalues in the S, A, H directions are $-\lambda_S, -\lambda_A, -\lambda_H < 0$ and are always negative. The stability of the steady states is therefore determined primarily by the blocks associated with the variables (C, E) and (T_A, T_B).

We first consider the completely healthy state E_0. The linearisation of (13)–(15) in a neighbourhood of $\mathbf{u} = 0$ has already been carried out above and yields three negative eigenvalues corresponding to the variables S, A, H. The subsystem in (C, E) at $T_A = T_B = A = H = 0$ takes the form

$$\dot{C} = -(k_e^0 + d_C)\, C + p_r E, \qquad \dot{E} = k_e^0 C - (p_r + d_E)\, E,$$

so that the Jacobian block corresponding to these variables takes the form

$$J_{CE}(E_0) = \begin{pmatrix} -(k_e^0 + d_C) & p_r \\ k_e^0 & -(p_r + d_E) \end{pmatrix}. \tag{32}$$

Its trace and determinant are given by

$$\operatorname{tr} J_{CE}(E_0) = -(k_e^0 + d_C) - (p_r + d_E) < 0,$$

$$\det J_{CE}(E_0) = (k_e^0 + d_C)(p_r + d_E) - p_r k_e^0 = k_e^0 d_E + d_C p_r + d_C d_E > 0.$$

It follows that both eigenvalues of the (C, E) block are negative, and small perturbations in the variables C, E decay.

For the tumour subsystem (T_A, T_B) in the neighbourhood of E_0, the logistic factor in (11), (12) is approximated as

$$r_T\Big(1 - \frac{T_A + T_B}{K_T}\Big) \approx r_T,$$

and interaction with CAR-T cells is absent, since $C^* = 0$. Taking into account $\mu_{AB}(0) = \mu_0$, $\mu_{BA}(0) = \mu_1$, we obtain the linear subsystem

$$\dot{T}_A = (r_T - d_{T_A} - \mu_0)\, T_A + \mu_1 T_B, \tag{33}$$

$$\dot{T}_B = \mu_0 T_A + (r_T - d_{T_B} - \mu_1)\, T_B. \tag{34}$$

The corresponding part of the Jacobian takes the form

$$J_T(E_0) = \begin{pmatrix} r_T - d_{T_A} - \mu_0 & \mu_1 \\ \mu_0 & r_T - d_{T_B} - \mu_1 \end{pmatrix}. \tag{35}$$

 doi:10.20944/preprints202603.0742.v1

The trace and determinant of this block are computed according to the equations

$$\operatorname{tr} J_T(E_0) = 2r_T - (d_{T_A} + d_{T_B} + \mu_0 + \mu_1), \tag{36}$$

$$\det J_T(E_0) = (r_T - d_{T_A} - \mu_0)(r_T - d_{T_B} - \mu_1) - \mu_0\mu_1. \tag{37}$$

The completely healthy steady state E_0 is locally asymptotically stable if

$$\operatorname{tr} J_T(E_0) < 0, \qquad \det J_T(E_0) > 0, \tag{38}$$

which guarantees that both eigenvalues of the block $J_T(E_0)$ are negative and, therefore, that tumour invasion is impossible.

Proposition 1. If conditions (38) are satisfied, the completely healthy steady state E_0 is locally asymptotically stable. Otherwise, there is at least one positive eigenvalue of the block $J_T(E_0)$, and small perturbations can drive the system away from E_0 allowing tumour growth.

Violation of conditions (38) leads to the emergence of a positive eigenvalue and renders the growth of the tumour population possible. Thus, conditions (36)–(38) define the boundary between the scenarios of tumour absence and tumour emergence in the model.

For the tumour steady state E_T, the stability with respect to CAR-T cell infiltration is of particular interest. Assuming that E_T is stable along the tumour coordinates (T_A, T_B, S, A, H) at $C = E = 0$ (a detailed analysis of the block $J_T(E_T)$ may be carried out analogously to the case of E_0), we linearise the (C, E) subsystem in a neighbourhood of E_T, while fixing

$$T_A^*, \quad T_B^*, \quad S^*, \quad A^*, \quad H^*$$

from (31), (21)–(23). Define

$$k_e^* = k_e(A^*, H^*), \qquad p_r^* = \frac{p_r}{1 + A^*}.$$

For small C, the non-linear growth of CAR-T cells

$$\rho_C \frac{CT_A}{K_C + C}$$

is linearised with respect to C as

$$\rho_C \frac{CT_A^*}{K_C + 0} = \frac{\rho_C}{K_C} T_A^* C.$$

The system for small perturbations in (C, E) then takes the form

$$\dot{C} = \left(\frac{\rho_C}{K_C} T_A^* - \delta_{CT} T_A^* - k_e^* - d_C\right) C + p_r^* E, \tag{39}$$

$$\dot{E} = k_e^* C - (p_r^* + d_E)\, E. \tag{40}$$

The corresponding part of the Jacobian takes the form

$$J_{CE}(E_T) = \begin{pmatrix} a_{11} & a_{12} \\ a_{21} & a_{22} \end{pmatrix}, \tag{41}$$

where

$$a_{11} = \frac{\rho_C}{K_C} T_A^* - \delta_{CT} T_A^* - k_e^* - d_C, \tag{42}$$

$$a_{12} = p_r^*, \tag{43}$$

$$a_{21} = k_e^*, \tag{44}$$

$$a_{22} = -(p_r^* + d_E), \tag{45}$$

 doi:10.20944/preprints202603.0742.v1

has a trace and determinant

$$\operatorname{tr} J_{CE}(E_T) = a_{11} + a_{22}, \tag{46}$$

$$\det J_{CE}(E_T) = a_{11}a_{22} - a_{12}a_{21}. \tag{47}$$

If these inequalities hold

$$\operatorname{tr} J_{CE}(E_T) < 0, \qquad \det J_{CE}(E_T) > 0, \tag{48}$$

then both eigenvalues of the matrix $J_{CE}(E_T)$ have negative real parts, small perturbations in the variables C, E decay, and the tumour state E_T is stable with respect to CAR-T cell infiltration. That is, small therapeutic doses do not lead to CAR-T cell persistence.

Proposition 2. Let the tumour steady state E_T exist and be stable along the tumour coordinates at $C = E = 0$. If conditions (48) are satisfied, then E_T is locally asymptotically stable with respect to small perturbations in C and E, and CAR-T cells cannot invade this state. In the case where

$$\max \operatorname{Re} \lambda\big(J_{CE}(E_T)\big) > 0,$$

the steady state E_T loses stability in the (C, E) direction, and a small population of CAR-T cells is able to invade the tumour state, which may lead either to tumour elimination or to the formation of a coexistence steady state E_{CT}.

From a biological point of view, the key determinant here is the term a_{11} (see (42)), which contains the expression that may be interpreted as the effective growth rate of functional CAR-T cells in the steady-state tumour microenvironment. Elevated levels of the immunosuppressive factors A^*, H^* lead to an increase in k_e^* and a decrease in p_r^*, thereby shifting the eigenvalues of the matrix $J_{CE}(E_T)$ towards negative real parts.

For the coexistence steady state E_{CT}, the full Jacobian

$$J(E_{CT}) = \frac{\partial F}{\partial \mathbf{u}}(E_{CT})$$

is a 7×7 matrix, and an analytical investigation of its spectrum becomes cumbersome. At the same time, owing to the linearity of the subsystem (S, A, H), the three eigenvalues corresponding to these variables remain equal to $-\lambda_S, -\lambda_A, -\lambda_H$ and are therefore negative. The signs of the real parts of the remaining eigenvalues are determined by the interaction of the populations C, E, T_A, T_B and, in the general case, must be determined numerically for fixed values of the model parameters.

The above analysis pertains to the spatially homogeneous version of the model and describes the stability of the homogeneous steady states of the full PDE system (1)–(7) with respect to homogeneous perturbations. Incorporating diffusion and chemotaxis may give rise to spatial instabilities, which may constitute a promising direction for further research.

2.3. Numerical Methods and Computational Implementation

For the numerical solution of the spatiotemporal system (1)–(7), a finite-difference approximation on a uniform rectangular three-dimensional grid was employed, with operator splitting by physical processes and a combined time-integration scheme.

The computational domain $\Omega = [0, L_x] \times [0, L_y] \times [0, L_z]$ is covered by a uniform grid

$$x_i = i\,\Delta x, \quad i = 0, 1, \ldots, N_x - 1, \tag{49}$$

$$y_j = j\,\Delta y, \quad j = 0, 1, \ldots, N_y - 1, \tag{50}$$

$$z_k = k\,\Delta z, \quad k = 0, 1, \ldots, N_z - 1, \tag{51}$$

 doi:10.20944/preprints202603.0742.v1

where the grid steps are equal

$$\Delta x = \frac{L_x}{N_x - 1}, \qquad \Delta y = \frac{L_y}{N_y - 1}, \qquad \Delta z = \frac{L_z}{N_z - 1}. \tag{52}$$

For all diffusion terms, the standard second-order central approximation is used. For an arbitrary variable $u \in C, E, T_A, T_B, S, A, H$, the three-dimensional Laplacian is approximated by a seven-point stencil

$$\begin{aligned}(\nabla^2 u)_{i,j,k} \approx \frac{u_{i+1,j,k} - 2u_{i,j,k} + u_{i-1,j,k}}{\Delta x^2} + \frac{u_{i,j+1,k} - 2u_{i,j,k} + u_{i,j-1,k}}{\Delta y^2} \\ + \frac{u_{i,j,k+1} - 2u_{i,j,k} + u_{i,j,k-1}}{\Delta z^2}.\end{aligned} \tag{53}$$

The chemotactic term in the equation for functional CAR-T cells is discretised in conservative form through fluxes across the cell faces

$$-\nabla \cdot (\chi_C(A)\, C\, \nabla S)\Big|_{i,j,k} \approx -\left(\frac{F^x_{i+\frac{1}{2},j,k} - F^x_{i-\frac{1}{2},j,k}}{\Delta x} + \frac{F^y_{i,j+\frac{1}{2},k} - F^y_{i,j-\frac{1}{2},k}}{\Delta y} + \frac{F^z_{i,j,k+\frac{1}{2}} - F^z_{i,j,k-\frac{1}{2}}}{\Delta z} \right), \tag{54}$$

where, for example, along the x-axis,

$$F^x_{i+\frac{1}{2},j,k} = \chi_{i+\frac{1}{2},j,k}\, C_{i+\frac{1}{2},j,k}\, \frac{S_{i+1,j,k} - S_{i,j,k}}{\Delta x}, \tag{55}$$

and the face values are computed as arithmetic averages

$$\chi_{i+\frac{1}{2},j,k} = \frac{\chi_C(A_{i,j,k}) + \chi_C(A_{i+1,j,k})}{2}, \qquad C_{i+\frac{1}{2},j,k} = \frac{C_{i,j,k} + C_{i+1,j,k}}{2}. \tag{56}$$

The fluxes along the y- and z-axes are defined analogously.

Reflecting boundary conditions are imposed for all variables at the domain boundary. In the software implementation, this is achieved through index handling: indices that fall outside the computational domain are replaced by the nearest boundary indices, which is equivalent to a zero normal derivative and zero flux across the boundary.

Let $U = (C, E, T_A, T_B, S, A, H)^\top$. The right-hand-side operator is represented as the sum

$$\frac{dU}{dt} = \mathcal{R}(U) + \mathcal{D}(U),$$

where $\mathcal{R}$ includes the reaction terms and chemotaxis, whereas $\mathcal{D}$ contains diffusion only. One time step Δt is computed using the Strang splitting scheme

$$U^{n+1} = \Phi_{\mathcal{R}}\left(\frac{\Delta t}{2}\right) \Phi_{\mathcal{D}}(\Delta t)\, \Phi_{\mathcal{R}}\left(\frac{\Delta t}{2}\right) U^n. \tag{57}$$

This scheme reduces the splitting error compared with simple first-order sequential splitting.

The operator $\mathcal{R}$ is integrated using an explicit two-stage second-order Runge–Kutta scheme. For a step of length h

$$K_1 = \mathcal{R}(U^m), \qquad K_2 = \mathcal{R}(U^m + hK_1), \tag{58}$$

$$U^{m+1} = U^m + \frac{h}{2}(K_1 + K_2). \tag{59}$$

The program code incorporates additional subdivision of the explicit step into substeps, which makes it possible to improve stability in the presence of stiff non-linear reaction and chemotactic terms.

 doi:10.20944/preprints202603.0742.v1

The diffusion part for each variable u is solved implicitly

$$\frac{u^* - u^{\text{rhs}}}{\tau} = D_u \nabla_h^2 u^*, \qquad \text{or} \qquad \left(I - \tau D_u \nabla_h^2\right) u^* = u^{\text{rhs}}, \tag{60}$$

where $\tau = \Delta t$, and D_u is the corresponding diffusion coefficient.

The resulting linear system is solved by the Jacobi iterative method. Denoting

$$a_x = \frac{\tau D_u}{\Delta x^2}, \qquad a_y = \frac{\tau D_u}{\Delta y^2}, \qquad a_z = \frac{\tau D_u}{\Delta z^2},$$

the iterative equation takes the form

$$u_{i,j,k}^{(m+1)} = \frac{b_{i,j,k} + a_x\left(u_{i+1,j,k}^{(m)} + u_{i-1,j,k}^{(m)}\right) + a_y\left(u_{i,j+1,k}^{(m)} + u_{i,j-1,k}^{(m)}\right) + a_z\left(u_{i,j,k+1}^{(m)} + u_{i,j,k-1}^{(m)}\right)}{1 + 2(a_x + a_y + a_z)}, \tag{61}$$

where $b_{i,j,k} = u_{i,j,k}^{\text{rhs}}$. The number of iterations and the stopping criterion are specified by the parameters `diff_iters` and `diff_tol`.

After the explicit and implicit substeps, a projection onto the physically admissible domain is applied to all components of the state

$$u_{i,j,k} \leftarrow \max(u_{i,j,k}, 0), \qquad u \in \{C, E, T_A, T_B, S, A, H\},$$

which excludes non-physical negative values arising from discretisation errors.

The algorithm for implementing a single complete computational experiment may be represented as follows:

Algorithm 1 Main computational loop of the solver

Require: Model parameters $\mathcal{P}$, domain dimensions (L_x, L_y, L_z), grid dimensions (N_x, N_y, N_z), time step Δt, final time T, `exp_substeps`, `diff_iters`, `diff_tol`, `output_every`
Ensure: The field states $U = (C, E, T_A, T_B, S, A, H)$, saved in `CSV` format

Construct a uniform grid; compute $\Delta x, \Delta y, \Delta z$
Initialise U^0
Save U^0 in `CSV` format
$N_t \leftarrow \lfloor T/\Delta t \rfloor$
for $n = 0, 1, \ldots, N_t - 1$ **do**
  $U \leftarrow \text{ReactionRK2}(U,\ \Delta t/2,\ \texttt{exp\_substeps})$
  for each component $u \in \{C, E, T_A, T_B, S, A, H\}$ **do**
    $b \leftarrow u$
    $u^{(0)} \leftarrow b$
    for $m = 0, 1, \ldots, \texttt{diff\_iters} - 1$ **do**
      $u_{\text{new}} \leftarrow \text{JacobiStep}\big((I - \Delta t\, \mathcal{L}_u)\, u = b,\ u^{(m)}\big)$
      $r_m \leftarrow \|u_{\text{new}} - u^{(m)}\|_\infty$
      $u^{(m+1)} \leftarrow u_{\text{new}}$
      if $r_m <$ `diff_tol` **then**
        break
      end if
    end for
    $u \leftarrow u^{(m+1)}$
  end for
  $U \leftarrow \text{ReactionRK2}(U,\ \Delta t/2,\ \texttt{exp\_substeps})$
  for each component $u \in \{C, E, T_A, T_B, S, A, H\}$ **do**
    $u \leftarrow \max(u, 0)$
  end for
  if $(n+1)$ mod `output_every` $= 0$ **then**
    Save the current fields U in `CSV`
  end if
end for
return saved files `CSV`

 doi:10.20944/preprints202603.0742.v1

The numerical solver was implemented in `C++`, using the `Params`, `Grid3D`, `Field`, and `State` structures to store the parameters, grid geometry, and model fields. To accelerate the computations, `OpenMP` parallelisation is employed in the loops over the grid nodes. The results are saved in `CSV` format. Each file contains the time, node indices, coordinates, and the values of all seven variables

$$(t, i, j, k, x, y, z, C, E, T_A, T_B, S, A, H),$$

which is convenient for subsequent visualisation and post-processing.

To describe the behaviour of the system, a normalised computational form of the model was used, in which the spatial coordinate, time, and population densities are represented by dimensionless variables.

To ensure reproducibility of the results, the full source code of the numerical solver has been made available in an open repository GitHub: https://github.com/maximvpolyakov/CAR-T-model (accessed on 6 March 2026).

3. Results

3.1. Typical Dynamics of the Spatially Homogeneous System Under Baseline Parameters

To obtain an integrated view of the model dynamics in the absence of spatial heterogeneity, this subsection presents a numerical investigation of the spatially homogeneous system (1)–(7), corresponding to the system of ordinary differential equations (9)–(15). This approach makes it possible to analyse the baseline behaviour of the model under standard parameter values without the influence of spatial migration and thereby to identify the key temporal patterns governing the interactions between functional and exhausted CAR-T cells, the antigen-positive and antigen-negative tumour subpopulations, and the microenvironmental fields.

The initial state considered was an antigenically homogeneous tumour composed predominantly of T_A cells, together with an initial administration of functional CAR-T cells. Although no antigen-negative population was present at the initial time, the structure of the model allows such a population to emerge during the course of evolution through the phenotypic transition $T_A \to T_B$, described by the function $\mu_{AB}(C)$. Thus, even in the spatially homogeneous case, the model makes it possible to investigate not only the direct cytotoxic action of CAR-T cells but also dynamically arising antigen escape.

The results of the numerical simulations are presented in Figure 3. As can be seen from the dynamics of the CAR-T populations, during the initial period after administration the functional cell population C exhibits a pronounced expansion phase, reaching a maximum at the early stages of evolution (Figure 3a). This reflects the predominance of antigen-dependent proliferation over natural death and exhaustion while the density of antigen-positive tumour cells remains high. However, as the exhausted subpopulation E accumulates and the phenotypic composition of the tumour changes, the level of C begins to decline and subsequently approaches a quasi-stationary plateau. At the same time, E increases monotonically and stabilises at a non-zero level, indicating the establishment of a persistent fraction of dysfunctional CAR-T cells in the system.

The dynamics of the tumour subpopulations are more complex (Figure 3b). The abundance of antigen-positive cells T_A decreases rapidly at the initial stage because of direct CAR-T-mediated lysis. However, complete eradication of this subpopulation is not achieved. After the phase of rapid decline, T_A approaches a low but positive level. At the same time, the antigen-negative subpopulation T_B, which is absent at the initial time point, begins to accumulate rapidly and eventually becomes the dominant component of the tumour. This behaviour directly reflects the action of the phenotypic-switching mechanism, whereby the selective pressure exerted by CAR-T cells promotes the transition of a fraction of tumour cells into an antigen-negative state that is less susceptible to therapy.

The integrated dynamics of the total tumour burden $T_A + T_B$ and the total CAR-T cell population $C + E$, shown in Figure 3c, further emphasise the presence of two successive phases in the system's evolution. During the first phase, a marked reduction in the overall tumour burden is observed, corresponding to an effective initial response to therapy. Subsequently, however, as the antigen-

 doi:10.20944/preprints202603.0742.v1

negative population becomes dominant, the total tumour burden begins to increase and ultimately approaches a high level close to its limiting value. By contrast, the total CAR-T cell population, after an initial expansion, gradually declines and stabilises at a lower level. Thus, the system exhibits a transition from a regime of short-term therapeutic control to one of partial immune equilibrium, in which CAR-T cells persist but are no longer capable of achieving complete suppression of the tumour population.

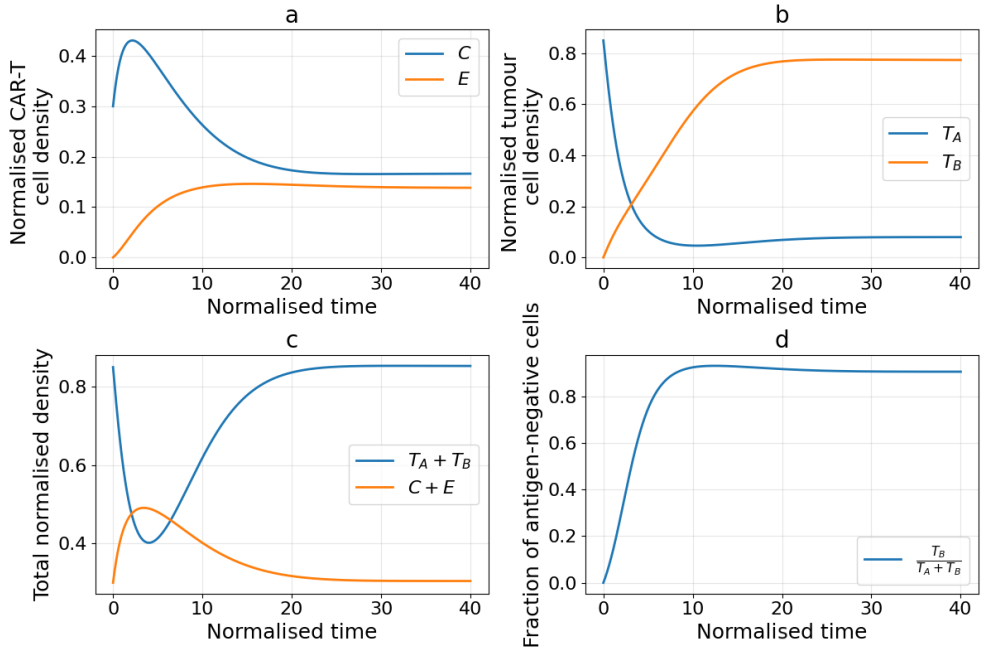

Figure 3. Typical dynamics of the spatially homogeneous system under baseline parameter values: (**a**) temporal evolution of the densities of functional C and exhausted E CAR-T cells; (**b**) temporal evolution of the densities of tumour cells with high T_A and low T_B expression of the target antigen; (**c**) dynamics of the total tumour burden $T_A + T_B$ and the total CAR-T cell density $C + E$; (**d**) proportion of antigen-negative tumour cells in the total tumour population $\frac{T_B}{T_A+T_B}$.

Particularly illustrative is the dynamics of the proportion of antigen-negative cells $\frac{T_B}{T_A+T_B}$ (Figure 3d). This quantity rapidly increases from zero to values close to unity, after which it stabilises at a high level. Thus, the spatially homogeneous system reproduces one of the most important qualitative effects of the model, namely the selection of the antigen-negative phenotype under CAR-T therapy. From a biological perspective, this corresponds to a scenario in which treatment efficiently eliminates the therapy-sensitive population but creates the conditions for the subsequent dominance of clones that escape immune recognition.

Taken together, the results indicate that, even under baseline parameter values and in the absence of spatial structure, the model exhibits non-trivial multistage behaviour. The initial phase of active CAR-T cell expansion and regression of the antigen-positive tumour is followed by a phase characterised by the accumulation of the exhausted effector population and the expansion of the antigen-negative subpopulation. As a consequence, the system tends towards neither complete tumour eradication nor complete disappearance of CAR-T cells, but instead approaches a coexistence regime characterised by a low but non-zero level of antigen-positive cells, dominance of the antigen-negative tumour population, and persistence of a residual CAR-T cell population. Thus, even in its spatially homogeneous formulation, the model already reproduces the key mechanisms embedded in the full spatiotemporal model.

3.2. Baseline Infiltration and Tumour Elimination in the Absence of Antigenic Heterogeneity

We consider the dynamics of the interaction between CAR-T cells and an antigenically homogeneous solid tumour in the absence of an antigen-negative subpopulation, that is, under the condition

 doi:10.20944/preprints202603.0742.v1

$T_B \equiv 0$ throughout the entire simulation interval. This formulation makes it possible to analyse in isolation the effects of spatial migration, chemotaxis, cytotoxicity, and CAR-T cell exhaustion on therapeutic outcome, without the additional contribution of antigen-escape mechanisms. Functional CAR-T cells C move by diffusion and chemotaxis along the gradient of the chemoattractant S, proliferate upon contact with antigen-positive tumour cells T_A, and simultaneously undergo exhaustion under the influence of the immunosuppressive factor A and hypoxia H. In this series of experiments, the tumour population is represented solely by T_A cells, for which logistic growth and sensitivity to CAR-T-mediated lysis are retained.

For the numerical analysis, a normalised version of the model was employed, in which all phase variables have comparable scales, thereby allowing clear visualisation of the CAR-T cell infiltration front and the subsequent tumour regression. The initial tumour distribution was specified as a localised spatial plateau, whereas the initial CAR-T cell population was placed near the boundary of the tumour focus, thereby modelling local administration of effector cells. The simulation was performed up to the time point $T = 12$ in dimensionless time. For the analysis of the results, the spatial profiles of T, C, and E at the final time point were considered, together with the integrated population characteristics and the spatiotemporal diagrams for functional CAR-T cells and the tumour population.

As shown in Figure 4a, a pronounced front of CAR-T cell infiltration into the tumour tissue is formed already at the early stages of the simulation. In the spatiotemporal diagram for C (see Figure 4c), a progressive advance of the region with elevated CAR-T cell density into the depth of the tumour can be observed, indicating an effective combination of diffusive migration and directed chemotaxis. At the same time, the functional population not only persists within the tissue but also expands, which points to a positive net balance between proliferation, natural death, and transition to the exhausted state. Consequently, under the regime considered, the effective growth rate of CAR-T cells in the tumour microenvironment remains positive, and the tumour itself is not stable with respect to infiltration by the effector population (see Figure 4d).

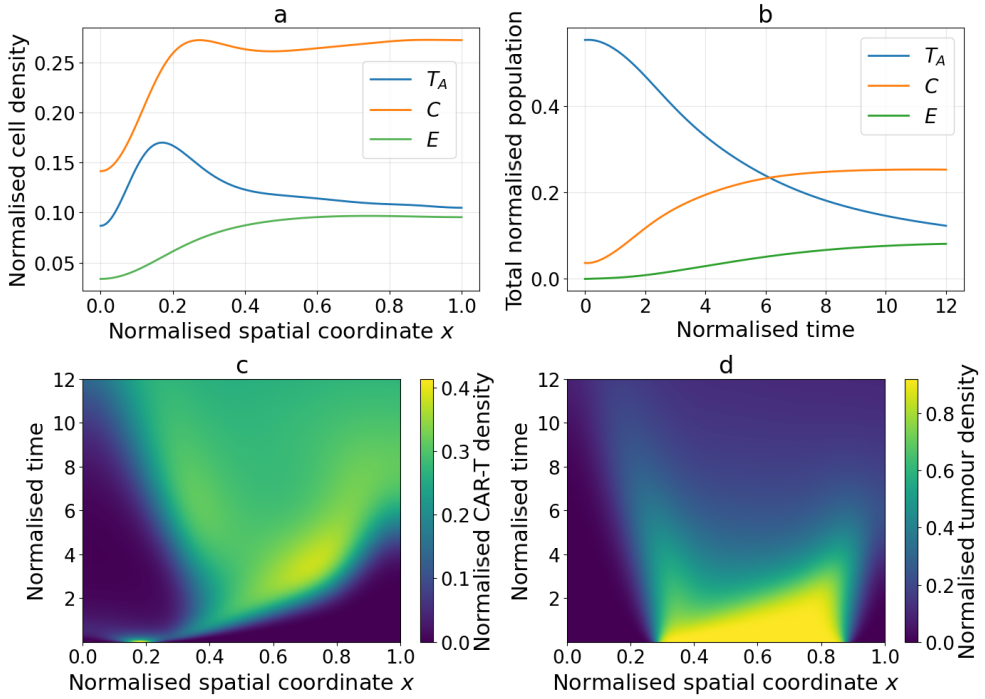

Figure 4. Results of the computational experiment simulating CAR-T cell infiltration and tumour elimination in the absence of antigenic heterogeneity ($T_B \equiv 0$): (**a**) spatial profiles of the densities of tumour cells T_A and the CAR-T cell populations C and E at the final simulation time; (**b**) temporal evolution of the spatially averaged (integrated) densities of T_A, C, and E; (**c**) spatiotemporal map of the density of functional CAR-T cells C; (**d**) spatiotemporal map of the density of tumour cells T_A.

 doi:10.20944/preprints202603.0742.v1

CAR-T cell infiltration is accompanied by a pronounced reduction in tumour burden. The integrated tumour mass decreases monotonically throughout the entire simulation interval, indicating that the cytotoxic effect of CAR-T cells dominates over the logistic growth of the tumour (see Figure 4b). At the same time, the integrated number of functional CAR-T cells increases during the early and intermediate stages and subsequently reaches a plateau. This behaviour reflects the transition of the system from a phase of active CAR-T cell expansion to a regime of partial saturation, in which the local reduction in tumour mass limits further antigen-dependent proliferation. A concurrent increase in the integrated density of exhausted cells is also observed; however, this increase remains slower than the accumulation of the functional population, with the result that exhaustion in this regime does not lead to loss of therapeutic control.

The final spatial profiles likewise confirm the efficacy of the therapy. By the time $t = 12$, functional CAR-T cells are distributed not only within the region of initial administration but also throughout the main tumour volume, indicating deep infiltration. The residual tumour density T is markedly reduced compared with the initial state, particularly in the regions of greatest CAR-T cell accumulation. At the same time, the distribution of E shows the formation of a non-zero exhausted subpopulation, localised predominantly in those regions where contact between CAR-T cells and the tumour has persisted for an extended period. Therefore, even in the absence of antigenic heterogeneity, the gradual exhaustion of the effector population within the tumour microenvironment remains a limiting factor for complete tumour eradication.

Thus, the results demonstrate that, in the baseline scenario without antigenic heterogeneity, the spatial model reproduces the biologically expected regime of successful CAR-T cell infiltration and partial tumour elimination. On the one hand, CAR-T cells form a sustained wave of infiltration into the tumour tissue and produce a substantial reduction in the total tumour burden. On the other hand, the accumulation of exhausted cells prevents complete tumour regression from being achieved over the selected time interval.

3.3. Effects of Antigenic Heterogeneity and Phenotypic Switching on Therapeutic Outcome

We next consider a computational experiment designed to investigate the effects of tumour antigenic heterogeneity and phenotypic switching between the antigen-positive and antigen-negative subpopulations on the efficacy of CAR-T therapy. In contrast to the baseline scenario, the initial tumour state here was specified as a mixture of T_A and T_B cells with different values of the proportion of the antigen-negative population $\frac{T_B}{T_A+T_B}$. This formulation is consistent with the structure of the model under consideration, in which CAR-T cells directly eliminate only the antigen-positive cells T_A, whereas antigen-negative cells T_B evade direct cytotoxic action and may accumulate during therapy through phenotypic transitions.

For the analysis, we consider the following switching scenarios: the baseline regime, a regime of accelerated antigen loss, and a regime of accelerated antigen recovery. In each scenario, the initial proportion of antigen-negative cells was varied as follows: 0, 0.2, and 0.5. The simulations were performed in the normalised computational formulation, which preserves the interaction structure of the full model, including CAR-T cell chemotaxis, proliferation, and exhaustion, as well as the combined contribution of both tumour subpopulations to the formation of an immunosuppressive microenvironment.

As can be seen from Figure 5, even in the baseline switching regime, an increase in the initial proportion of T_B leads to a systematic deterioration in therapeutic response. At low values of $T_B(0)$, a pronounced initial regression of the total tumour burden $T_A + T_B$ is observed; however, as the initial proportion of the antigen-negative subpopulation increases, the depth of this regression decreases, whereas the subsequent tumour regrowth becomes more pronounced. Thus, antigenic heterogeneity manifests itself not only as a static factor of resistance but also as a dynamic mechanism that reduces the efficacy of CAR-T-mediated tumour control even when substantial infiltration of effector cells into the tumour tissue is maintained.

 doi:10.20944/preprints202603.0742.v1

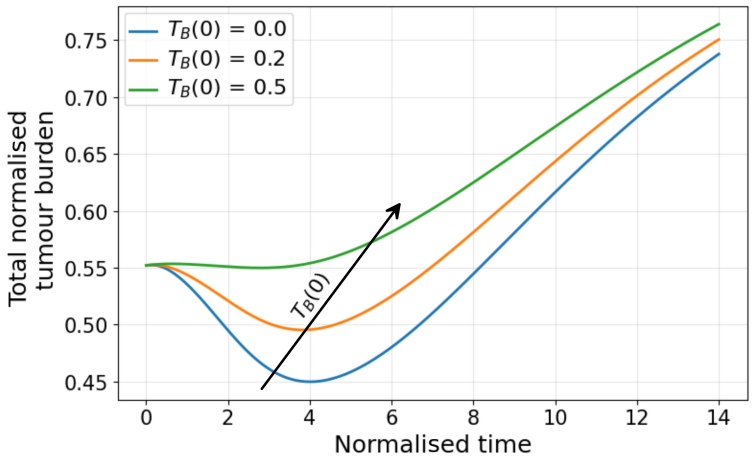

Figure 5. Temporal evolution of the total tumour burden $T_A + T_B$ for different initial proportions of antigen-negative cells $T_B(0)$ (with all other model parameters held fixed).

The summary relationships between the final tumour mass and the final proportion of antigen-negative cells as functions of the initial value $\frac{T_B(0)}{T_A(0)+T_B(0)}$ are presented in Figure 6. In all scenarios considered, an increase in the initial proportion of T_B leads to an increase in the residual tumour burden by the end of the simulation. The poorest outcomes correspond to the rapid-loss regime, in which accelerated antigen loss enhances selection of the T_B phenotype and increases the final tumour mass. By contrast, the rapid-recovery scenario yields the lowest values of residual tumour burden and a lower final proportion of T_B, indicating partial restoration of tumour sensitivity to CAR-T-mediated lysis through the reverse transition of a fraction of cells to the antigen-positive state.

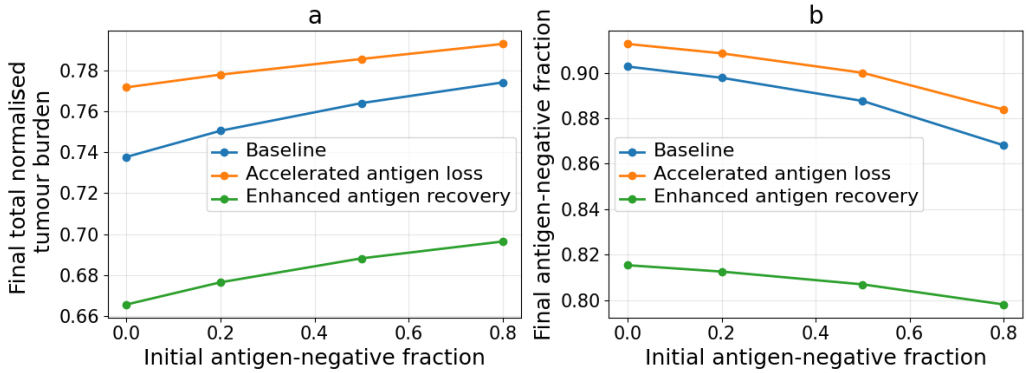

Figure 6. Effects of antigenic heterogeneity and phenotypic switching on therapeutic outcome: (**a**) final total tumour burden $T_A + T_B$ as a function of the initial proportion of antigen-negative cells $\frac{T_B(0)}{T_A(0)+T_B(0)}$ for the baseline scenario and two switching variants (accelerated antigen loss and enhanced antigen recovery); (**b**) final proportion of antigen-negative cells $\frac{T_B}{T_A+T_B}$ as a function of the initial proportion $\frac{T_B(0)}{T_A(0)+T_B(0)}$ for the same scenarios.

The spatiotemporal structure of the process is shown in Figure 7 for a representative case of the baseline regime with moderate initial heterogeneity. The integrated curves indicate that, during therapy, the population T_A decreases monotonically, whereas the population T_B increases and eventually comes to dominate the total tumour burden. At the same time, the total number of functional CAR-T cells C increases at the initial stage and subsequently reaches a plateau, while the exhausted subpopulation E gradually accumulates. This behaviour indicates that CAR-T cells retain their capacity for infiltration and expansion; however, their antitumour activity becomes increasingly constrained by the phenotypic shift of the tumour towards the antigen-negative state.

By the final time point, the residual density of T_A remains comparatively low throughout the tumour volume, whereas the distribution of T_B forms the dominant plateau. At the same time, the profile of C shows the persistence of functional CAR-T cells within the tissue, indicating that the reduction in therapeutic efficacy in this case is not associated with the complete disappearance of

 doi:10.20944/preprints202603.0742.v1

the effector population. On the contrary, the proportion $\frac{T_B}{T_A+T_B}$ demonstrates the progressive spread of the antigen-negative phenotype both over time and across space. This means that the principal mechanism underlying the loss of tumour control is antigen escape itself, rather than inadequate CAR-T cell infiltration.

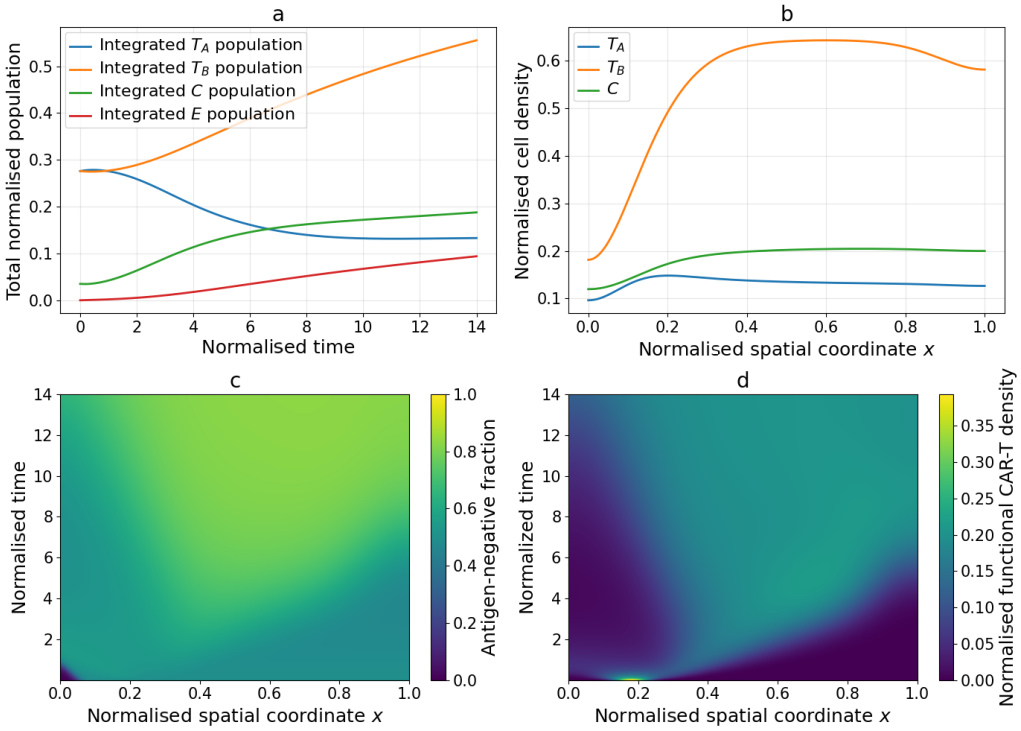

Figure 7. Effects of antigenic heterogeneity and phenotypic switching on the spatiotemporal dynamics: (**a**) temporal evolution of the spatially averaged populations T_A, T_B, C, and E; (**b**) spatial profiles of the densities of tumour cells T_A and T_B and of functional CAR-T cells C at the final simulation time; (**c**) spatiotemporal map of the proportion of antigen-negative tumour cells $\frac{T_B}{T_A+T_B}$; (**d**) spatiotemporal map of the density of functional CAR-T cells C.

These results show that initial antigenic heterogeneity and therapy-induced phenotypic switching can qualitatively alter the outcome of CAR-T therapy. Even in regimes in which CAR-T cells successfully infiltrate the tumour and establish a sustained active population, the presence of an antigen-negative subpopulation leads to a reduced depth of response and an increased residual tumour burden. Acceleration of antigen loss further amplifies this effect, whereas an increase in the rate of the reverse transition $T_B \to T_A$ partially restores tumour sensitivity to therapy. Consequently, within the framework of the present model, antigenic heterogeneity emerges as one of the central mechanisms of therapeutic resistance and should be regarded as a key factor when assessing the potential efficacy of CAR-T-based approaches for solid tumours.

3.4. Effects of the Immunosuppressive Factor and Hypoxia on the Efficacy of CAR-T Therapy

We investigated the effects of the immunosuppressive factor A and hypoxia H on the efficacy of CAR-T therapy in a spatiotemporal model of a solid tumour. Unlike the experiment involving antigenic heterogeneity, the present case considered an antigenically homogeneous tumour focus, which made it possible to analyse in isolation the contribution of the microenvironment to the formation of the therapeutic response.

In the model, the biochemical fields are linked to the tumour population through a dual action. The chemoattractant S is produced by antigen-positive tumour cells and provides the signal for CAR-T cell migration, whereas the immunosuppressive factor A is produced by the tumour and is further amplified in hypoxic regions through the term $\sigma_M f(H)$. Hypoxia H, in turn, increases in proportion to the tumour burden and is attenuated by perfusion and buffering processes. Thus, the tumour

 doi:10.20944/preprints202603.0742.v1

establishes a self-sustaining suppressive microenvironment that limits both CAR-T cell infiltration and their long-term functionality.

For the numerical analysis, the following scenarios were considered: a baseline regime, an enhanced-microenvironment regime, and a combined-intervention regime. In the enhanced-microenvironment scenario, the sources of immunosuppression and hypoxia were increased, while the corresponding decay coefficients were simultaneously reduced, thereby modelling a more aggressive tumour microenvironment. By contrast, in the combined-intervention scenario, the intensity of formation of the A and H fields was reduced, the rates of their removal were increased, and a repeated infusion of CAR-T cells was added, thereby modelling a combined therapeutic strategy. In all cases, the same initial tumour configuration and the same spatial formulation with Neumann boundary conditions on the boundary of the computational domain were used.

The overall comparative results for the different scenarios are presented in Figure 8. In all cases, a reduction in the total tumour burden is observed during the initial period; however, the depth and durability of the response depend substantially on the properties of the microenvironment. The poorest therapeutic outcome corresponds to the enhanced-microenvironment scenario. Under this regime, the largest residual tumour burden remains by the end of the simulation. By contrast, the combined-intervention regime achieves the most pronounced reduction in tumour burden. The baseline scenario occupies an intermediate position, demonstrating partial tumour control but without the maximal therapeutic effect.

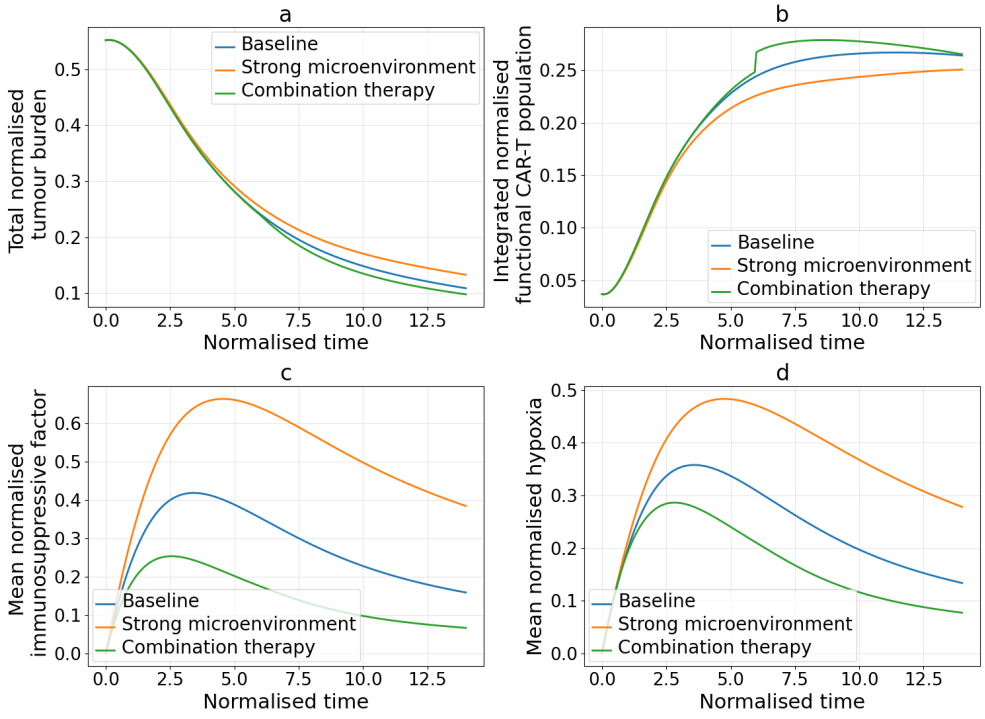

Figure 8. Effects of the microenvironment and combination therapy on system dynamics: (**a**) temporal evolution of the total tumour burden $T_A + T_B$ for the baseline scenario, the enhanced immunosuppressive–hypoxic microenvironment, and combination therapy; (**b**) temporal evolution of the spatially averaged density of functional CAR-T cells; (**c**) temporal evolution of the domain-averaged concentration of the immunosuppressive factor A; (**d**) temporal evolution of the domain-averaged degree of hypoxia H.

In the baseline regime, and especially in the combination-therapy scenario, the integrated number of functional CAR-T cells increases during the early and intermediate stages, indicating successful infiltration and antigen-dependent expansion. In the enhanced immunosuppressive–hypoxic microenvironment scenario, the growth of the CAR-T cell population is less pronounced, and its total level remains lower than in the other two cases. At the same time, combination therapy produces an additional increase in C following repeated infusion, accompanied by a further enhancement of the

 doi:10.20944/preprints202603.0742.v1

antitumour effect. Thus, attenuation of the adverse influence of the microenvironment and maintenance of the effector population act synergistically. The step-like change in Figure 8b corresponds to the moment of discrete intervention in the combination-therapy scenario, implemented as a single instantaneous change in the system state. As a result, the integrated characteristic of the functional population undergoes an immediate increase, which appears as a step in the graph.

The key difference between the scenarios is determined by the dynamics of the A and H fields themselves. In the enhanced immunosuppressive–hypoxic microenvironment scenario, the mean levels of the immunosuppressive factor and hypoxia reach their highest values and remain elevated throughout a substantial part of the simulation. This means that CAR-T cells are exposed for prolonged periods to conditions of weakened chemotaxis and increased exhaustion. In the baseline regime, the peaks of A and H are of moderate magnitude, whereas under combination therapy they are markedly lower and decline more rapidly over time. Thus, the numerical results confirm that the level of the immunosuppressive microenvironment is not merely an accompanying characteristic of the tumour, but one of the determining factors of therapeutic outcome.

The spatiotemporal structure of the process is shown in Figures 9 and 10. In the baseline regime, a typical scenario of partial tumour control is observed. The CAR-T cell population infiltrates the tumour tissue, and the total tumour burden decreases monotonically; however, the exhausted subpopulation E accumulates simultaneously, while the fields A and H attain appreciable values within the tumour volume. The spatial distributions of A and H show that the regions of maximal immunosuppression and hypoxia are formed inside the tumour focus and persist for as long as a substantial tumour burden remains. This indicates the existence of a negative feedback loop in which the tumour, even while decreasing under the action of CAR-T cells, temporarily sustains conditions that impair the effectiveness of further immune attack.

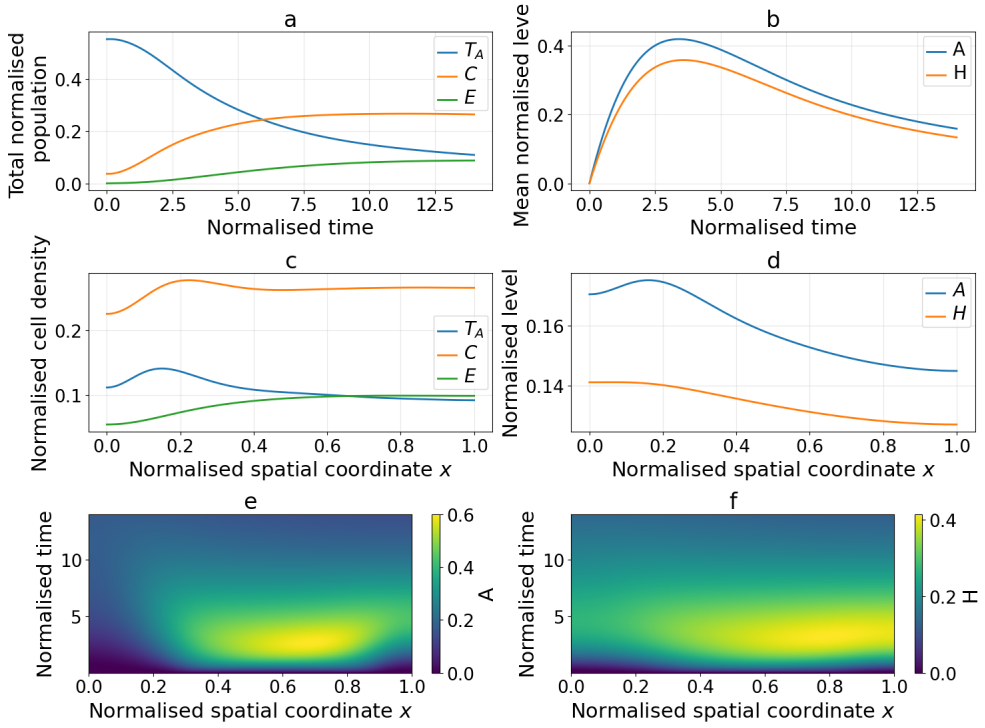

Figure 9. Spatiotemporal dynamics of cellular populations and microenvironmental factors in the baseline scenario: (**a**) temporal evolution of the spatially averaged (integrated) populations of tumour cells T_A and CAR-T cells C and E; (**b**) temporal evolution of the domain-averaged levels of the immunosuppressive factor A and hypoxia H; (**c**) spatial profiles of the densities T_A, C, and E at the final simulation time; (**d**) spatial profiles of the levels of A and H at the final simulation time; (**e**) spatiotemporal map of the immunosuppressive factor A; (**f**) spatiotemporal map of hypoxia H.

 doi:10.20944/preprints202603.0742.v1

In the combination-therapy scenario, the spatial pattern changes qualitatively. Following repeated CAR-T cell infusion, an additional increase in the effector population is observed, while the levels of A and H remain substantially lower than in the baseline regime. Accordingly, the final spatial profiles show a lower residual tumour density and a more favourable balance between functional and exhausted CAR-T cells. The spatial distributions indicate that the immunosuppressive microenvironment does not have sufficient time to develop to levels comparable to those in the baseline or enhanced scenario and therefore does not block the further advance of CAR-T cells into the tissue. This confirms that simultaneous targeting of the microenvironment and maintenance of the CAR-T cell pool may serve as an effective strategy for enhancing therapy.

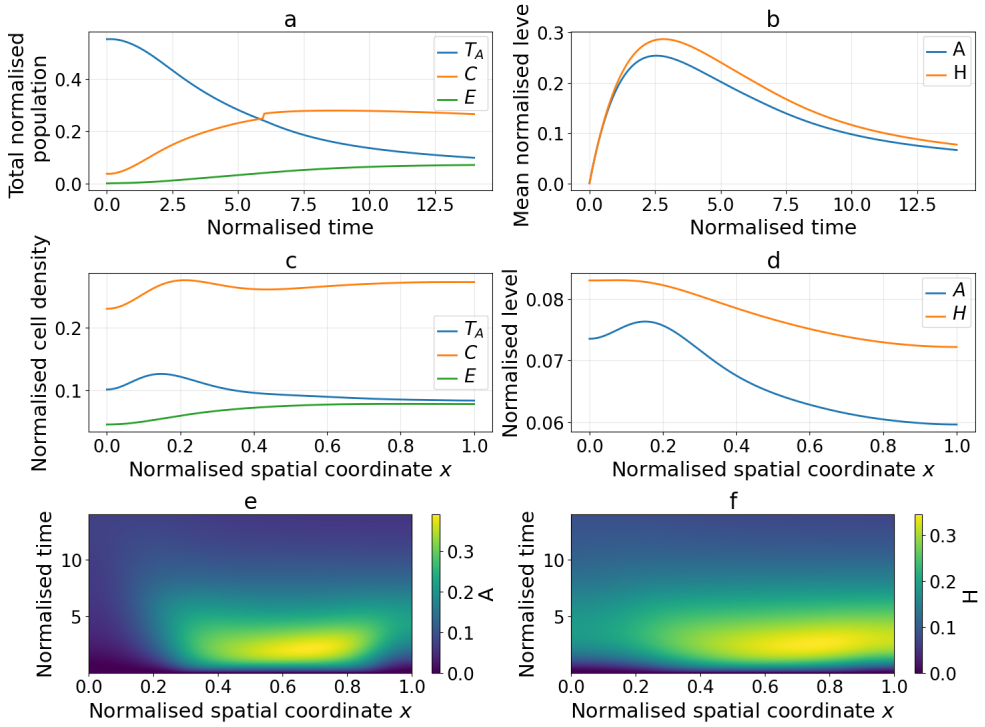

Figure 10. Spatiotemporal dynamics of cellular populations and microenvironmental factors in the combination-therapy scenario: (**a**) temporal evolution of the spatially averaged (integrated) populations of tumour cells T_A and CAR-T cells C and E; (**b**) temporal evolution of the domain-averaged levels of the immunosuppressive factor A and hypoxia H; (**c**) spatial profiles of the densities T_A, C, and E at the final simulation time; (**d**) spatial profiles of the levels of A and H at the final simulation time; (**e**) spatiotemporal map of the immunosuppressive factor A; (**f**) spatiotemporal map of hypoxia H.

The results obtained are in good agreement with the analytical conclusions derived from the spatially homogeneous model, according to which an increase in the steady-state levels of the immunosuppressive factors A and H raises the effective rate of CAR-T cell exhaustion and reduces the likelihood of their successful invasion of the tumour state. In the computational experiments considered here, this is manifested by the fact that enhancement of the microenvironment shifts the system towards a less favourable regime with a higher residual tumour burden, whereas attenuation of the microenvironment and repeated CAR-T cell infusion, by contrast, expand the region of parameter space in which sustained therapeutic control is achieved.

Thus, the numerical simulations show that the immunosuppressive factor and hypoxia are critical regulators of the outcome of CAR-T therapy for solid tumours. Their intensification leads to weakened chemotaxis, increased exhaustion of the effector population, and impaired tumour control. Conversely, reduction of the suppressive microenvironment and combined support of CAR-T cells result in more pronounced tumour regression and more durable preservation of functional antitumour activity. These findings support the inclusion of microenvironmental parameters among the key targets for optimising CAR-T therapy for solid tumours.

 doi:10.20944/preprints202603.0742.v1

4. Discussion

The results obtained indicate that, within the proposed model, the efficacy of CAR-T therapy for solid tumours is determined not by an isolated enhancement of cytotoxicity, but by the coordination of several interrelated processes: the spatial accessibility of tumour tissue to effector cells, the preservation of the functional state of CAR-T cells, and the stability of the tumour antigenic profile under therapeutic pressure. Accordingly, the therapeutic response should be regarded as the outcome of a dynamic interplay between infiltration, exhaustion, and antigen escape, rather than as a direct function of the initial dose of the cellular product. This conclusion is particularly important in the context of solid tumours, where spatial barriers and microenvironmental features may qualitatively alter the trajectory of response even in the presence of an initially active effector population [6,7,34,46].

From a mechanistic perspective, the model shows that early expansion and infiltration of CAR-T cells do not, in themselves, guarantee durable tumour control. A key limiting factor is the transition of a fraction of the effector population into a dysfunctional state. Exhaustion reduces not only the immediate cytotoxic activity, but also the capacity of the system to sustain the spatial front of antitumour action. In other words, the loss of functional competence in CAR-T cells acts as an intrinsic brake on the therapeutic wave, particularly in regions where the microenvironment simultaneously enhances exhaustion and weakens the migratory response. This is consistent with current views on the central role of T-cell exhaustion in the failure of CAR-T therapy for solid tumours [8,59], as well as with data on hypoxia-responsive CAR-T cells, in which adaptation to the hypoxic niche is associated with less pronounced exhaustion and greater antitumour activity [62]. Thus, the model results further emphasise that hypoxia and metabolic constraints should be regarded not as background conditions, but as active regulators of therapeutic outcome.

Equally important is the interpretation of antigenic heterogeneity. In the present formulation, the antigen-negative or antigen-low population acts not only as a pre-existing subclone, but also as a dynamically maintained tumour state stabilised by therapeutic pressure. Accordingly, the deterioration in response observed with an increased transition $T_A \to T_B$ should be interpreted as a manifestation of adaptive tumour evolution, rather than solely as the selection of pre-existing variants. In this sense, resistance is determined not only by the presence of heterogeneity, but also by the tumour's capacity to redistribute phenotypes towards reduced immune vulnerability. This conclusion is consistent with studies in which antigenic heterogeneity and antigen-dependent escape are regarded as key mechanisms underlying relapse and incomplete response [9,36,61]. At the same time, it supports interest in more advanced engineered recognition strategies, including dual-gated and inducible dual CAR constructs, which make it possible to broaden targeting selectivity while simultaneously reducing the risk of off-tumour toxicity [63].

The role of the immunosuppressive factor and hypoxia in the model is likewise of fundamental importance. Together, they establish a positive feedback loop: tumour burden promotes the accumulation of a suppressive microenvironment, which in turn reduces the efficacy of the antitumour response by weakening CAR-T cell migration and enhancing their exhaustion. Thus, hypoxia, soluble inhibitory signals, and the spatial organisation of the tissue become active determinants of treatment outcome. This is consistent with published experimental and theoretical evidence indicating that the principal barrier to CAR-T therapy for solid tumours lies not only in antigen selection, but also in the inability to sustain an effective presence of effector cells within the tumour in the context of pronounced immunosuppression [3,4,6,7]. From a spatial perspective, our conclusions are aligned with studies showing that tumour geometry, the mode of cell delivery, and the spatiotemporal structure of the microenvironment substantially alter the probability of therapeutic success [34,46]. However, unlike models that focus primarily on transport and cytotoxicity, the proposed system links spatial dynamics with tumour phenotypic plasticity and reversible CAR-T cell exhaustion, thereby making it possible to explain not only the occurrence of therapeutic failure itself, but also the transition from an early response to sustained incomplete control.

 doi:10.20944/preprints202603.0742.v1

From a theoretical perspective, the proposed model shows that CAR-T therapy for solid tumours cannot be adequately described by considering effector-population kinetics, tumour antigenic structure, or spatial transport in isolation. A substantial contribution of the present work lies in integrating these processes within a unified reaction–diffusion–chemotaxis framework with phenotypic switching and microenvironment-dependent exhaustion. Such a formalisation makes it possible to move beyond a simple enumeration of barriers towards an analysis of their combined action and, consequently, towards a more rigorous formulation of the problem of identifying therapeutic regimes in which infiltration can outpace the development of a resistant and immunosuppressive tumour state [31,39,40]. From a practical perspective, the results indicate that rational optimisation of therapy should involve not only target selection, but also the deliberate modification of the conditions governing CAR-T cell function within the tumour. This applies both to strategies aimed at enhancing homing and infiltration, in line with evidence of improved efficacy of HER2-CAR T cells upon co-expression of CXCR5/CCR6 [64], and to armoured approaches designed to increase resistance to TGF-β- and PD-L1-dependent immunosuppression [65]. In this context, the most promising solutions appear to be not monofactorial interventions, but multi-target engineering strategies that simultaneously improve trafficking, functional resilience, and recognition selectivity.

Despite its biological relevance, the model has a number of limitations. First, the immunosuppressive microenvironment is represented by a generalised variable A that aggregates several molecularly distinct mechanisms of suppression. This approach is convenient for conceptual analysis, but it does not allow the respective contributions of TGF-β, IL-10, the adenosine pathway, PD-L1 signalling, and other components to be distinguished, even though these may require different therapeutic interventions. In addition, the antigenic structure of the tumour is reduced to two phenotypic states, whereas in real tumours target expression more often forms a continuum and depends on local microenvironmental conditions and therapeutic pressure [36]. The model also does not include an explicit description of the vascular network, extracellular matrix, mechanical constraints of the tissue, or endogenous immune populations, although these factors largely determine tumour accessibility to cellular therapy and the magnitude of bystander effects [9,35]. Finally, the analysis is performed in a deterministic framework and therefore does not capture stochastic effects associated with rare clones, variability of the cellular product, or inter-patient heterogeneity in parameter values. For this reason, quantitative predictions should be interpreted with caution until specific calibration has been carried out using experimental or clinical data.

Future work may proceed in several directions. First, the model could be extended towards a more detailed description of antigen expression, vascular perfusion, metabolic constraints, and the extracellular matrix. Second, it should be calibrated against spatially resolved data, including tumour-on-a-chip platforms, microfluidic systems, and spatial biology datasets [33,43]. Third, the model may be expanded to analyse specific CAR-T cell engineering strategies, including hypoxia-responsive, dual-gated, homing-enhanced, and armoured approaches [62–65]. Fourth, its use for the optimisation of combination therapy appears particularly promising, as contemporary mathematical studies indicate that the efficacy of combining CAR-T cells with other modalities, including oncolytic viruses, depends substantially on the interaction kinetics of the components and on the schedule of their administration [66].

Thus, the principal contribution of the present study lies in proposing a mechanistically coherent spatiotemporal framework in which infiltration, exhaustion, antigen escape, and the suppressive microenvironment are treated as elements of a single dynamic system. This makes it possible to explain more precisely why even a biologically active cellular product may fail to achieve sustained control of a solid tumour, while at the same time identifying the most well-founded directions for further therapeutic optimisation: reduction of immunosuppression, improvement of cellular trafficking, limitation of antigen escape, and the rational combination of CAR-T therapy with additional therapeutic interventions. In this sense, the proposed model represents not only a tool for interpreting

 doi:10.20944/preprints202603.0742.v1

the results obtained, but also a foundation for the development of more realistic personalised in silico platforms for optimising CAR-T therapy for solid tumours.

5. Conclusions

In this study, a spatiotemporal mathematical model of CAR-T therapy for solid tumours was developed and analysed, incorporating antigenic heterogeneity, phenotypic switching of tumour cells, functional exhaustion of CAR-T cells, and the influence of the immunosuppressive and hypoxic microenvironment. The aim of the study was to identify the key factors governing CAR-T cell infiltration, therapeutic efficacy, and the mechanisms of tumour escape in spatially heterogeneous tissue.

The analysis showed that therapeutic outcome is determined by the combined action of three principal processes: CAR-T cell infiltration into the tumour, preservation of their functional activity, and the resilience of the antigen-positive tumour population to therapeutic pressure. The model reproduces a biologically plausible regime in which a substantial reduction in tumour burden may coexist with incomplete eradication as a consequence of CAR-T cell exhaustion, and demonstrates that antigen-negative subpopulations and therapy-induced antigen loss reduce treatment efficacy and contribute to the persistence of residual disease. In addition, the results indicate the critical limiting role of the immunosuppressive and hypoxic microenvironment, which weakens the migration and persistence of effector cells.

The principal conclusion of this study is that resistance of solid tumours to CAR-T therapy arises from the joint dynamics of spatial infiltration, phenotypic tumour adaptation, and microenvironment-mediated loss of effector function. The main contribution of this work lies in the development of a mechanistically consistent in silico platform that makes it possible to analyse these processes within a unified reaction–diffusion–chemotaxis framework and to serve as a foundation for the further computational evaluation of therapeutic strategies for solid tumours.

Funding: The study was funded by the Russian Science Foundation grant No. 25-71-00041, https://rscf.ru/project/25-71-00041/ (accessed on 6 March 2026).

Data Availability Statement: The original contributions presented in this study are included in the article. Further inquiries can be directed to the corresponding author.

Conflicts of Interest: The author declares no conflicts of interest.

References

1. Maude, S.L.; Frey, N.; Shaw, P.A. et al. Chimeric antigen receptor T cells for sustained remissions in leukemia. *N. Engl. J. Med.* **2014**, *371(16)*, 1507–1517.
2. Neelapu, S.S.; Locke, F.L.; Bartlett, N.L. et al. Axicabtagene ciloleucel CAR T-cell therapy in refractory large B-cell lymphoma. *N. Engl. J. Med.* **2017**, *377(26)*, 2531–2544.
3. Newick, K.; O'Brien, S.; Moon, E. et al. CAR T cell therapy for solid tumors. *Annu. Rev. Med.* **2016**, *68*, 139–152.
4. Wagner, J.; Wickman, E.; DeRenzo, C. et al. CAR T cell therapy for solid tumors: bright future or dark reality? *Mol. Ther.* **2020**, *28(11)*, 2320–2339.
5. Larson, R.C.; Maus, M.V. Recent advances and discoveries in the mechanisms and functions of CAR T cells. *Nat. Rev. Cancer* **2021**, *21*, 145–161.
6. Hou, A.J.; Chen, L.C.; Chen, Y.Y. Navigating CAR-T cells through the solid-tumour microenvironment. *Nat. Rev. Drug Discov.* **2023**, *20(7)*, 531–550.
7. Gumber, D.; Wang, L.D. Improving CAR-T immunotherapy: Overcoming the challenges of T cell exhaustion. *EBioMedicine* **2022**, *77*, 103941.
8. Guedan, S.; Ruella, M.; June, C.H. Emerging cellular therapies for cancer. *Annu. Rev. Immunol.* **2019**, *37*, 145–171.
9. Kara, E.; Jackson, T.L.; Jones, C. et al. Mathematical modeling insights into improving CAR T cell therapy for solid tumors with bystander effects. *npj Syst. Biol. Appl.* **2024**, *10*, 105.

 doi:10.20944/preprints202603.0742.v1

10. Polyakov, M.V.; Tuchina, E.I. Reaction-Diffusion Model of CAR-T Cell Therapy in Solid Tumours with Antigen Escape. *Computation* **2026**, *14(1)*, 3.
11. Enderling, H.; Chaplain, M.A.J. Mathematical modeling of tumor growth and treatment. *Curr. Pharm. Des.* **2014**, *20(30)*, 4934–4940.
12. De Pillis, L.G.; Radunskaya, A.E. The dynamics of an optimally controlled tumor model: A case study. *Math. Comput. Model.* **2003**, *37(11)*, 1221-1244.
13. Byrne, H.M. Dissecting cancer through mathematics: from the cell to the animal model. *Nat. Rev. Cancer* **2010**, *10*, 221–230.
14. Anderson, A.R.A. A hybrid mathematical model of solid tumour invasion: the importance of cell adhesion. *Math. Med. Biol.* **2005**, *22(2)*, 163–186.
15. Lorenzo, G. et al. Patient-specific, mechanistic models of tumor growth incorporating artificial intelligence and big data. *Annu. Rev. Biomed. Eng.* **2024**, *26(1)*, 529–560.
16. Araujo, R.P.; McElwain, D.L.S. A history of the study of solid tumour growth: The contribution of mathematical modelling. *Bull. Math. Biol.* **2004**, *66*, 1039–1091.
17. Rejniak, K.A.; Anderson, A.R.A. Hybrid models of tumor growth. *Wiley Interdiscip. Rev. Syst. Biol. Med.* **2011**, *3(1)*, 115–125.
18. Golmankhaneh, A.K. et al. Modeling tumor growth using fractal calculus: Insights into tumor dynamics. *Biosystems* **2024**, *235*, 105071.
19. Kamran, M.; Abdullah, J.Y.; Ahmad Satmi, A.S.; Genisa, M.; Majeed, A.; Nadeem, T. Mathematical Modeling and Analysis of Tumor Growth Models Integrating Treatment Therapy. *Math. Comput. Appl.* **2025**, *30(6)*, 119.
20. Polyakov, M.V.; Ten, V.V. Simulation tumor growth in heterogeneous medium based on diffusion equation. *Int. J. Mod. Phys. C* **2024**, *35(1)*, 2450010.
21. Swan, G.W. Role of optimal control theory in cancer chemotherapy. *Math. Biosci.* **1990**, *101*, 237–284.
22. van Genderen, M.N.G.; Kneppers, J.; Zaalberg, A. et al. Agent-based modeling of the prostate tumor microenvironment uncovers spatial tumor growth constraints and immunomodulatory properties. *npj Syst. Biol. Appl.* **2024**, *10*, 20.
23. Eftimie, R.; Bramson, J.L.; Earn, D.J.D. Interactions between the immune system and cancer: A brief review of non-spatial mathematical models. *Bull. Math. Biol.* **2011**, *73*, 2–32.
24. Mallet, D.G.; De Pillis, L.G. A cellular automata model of tumor-immune system interactions. *J. Theor. Biol.* **2006**, *239(3)*, 334–350.
25. Kuznetsov, V.A.; Makalkin, I.A.; Taylor, M.A. et al. Nonlinear dynamics of immunogenic tumors: Parameter estimation and global bifurcation analysis. *Bull. Math. Biol.* **1994**, *56(2)*, 295–321.
26. d'Onofrio, A. A general framework for modeling tumor-immune system competition and immunotherapy: Mathematical analysis and biomedical inferences. *Physica D: Nonlinear Phenomena* **2005**, *208(3-4)*, 220–235.
27. de Pillis, L.G.; Radunskaya, A.E.; Wiseman, C.L. A validated mathematical model of cell-mediated immune response to tumor growth. *Cancer Res.* **2005**, *65(17)*, 7950–7958.
28. Wilkie, K.P. A review of mathematical models of cancer-immune interactions in the context of tumor dormancy. *Adv. Exp. Med. Biol.* **2013**, *734*, 201–234.
29. Kimmel, G.J.; Locke, F.L.; Altrock, P.M. The roles of T cell competition and stochastic extinction events in chimeric antigen receptor T cell therapy. *Proc. Biol. Sci.* **2021**, *288(1947)*, 20210229.
30. Sabir, S.; León-Triana, O.; Serrano, S. et al. Mathematical Model of CAR T-Cell Therapy for a B-Cell Lymphoma Lymph Node. *Bull Math Biol* **2025**, *87*, 40.
31. Murias-Closas, A. et al. Computational modelling of CAR T-cell therapy: from cellular kinetics to patient-level predictions. *EBioMedicine* **2025**, *113*, 105597.
32. Paixão, E.A.; Barros, L.R.C.; Fassoni, A.C.; Almeida, R.C. Modeling Patient-Specific CAR-T Cell Dynamics: Multiphasic Kinetics via Phenotypic Differentiation. *Cancers* **2022**, *14*, 5576.
33. Adriani, G.; Pavesi, A.; Tan, A.T.; Bertoletti, A.; Thiery, J.P.; Kamm, R.D. Microfluidic models for adoptive cell-mediated cancer immunotherapies. *Drug Discov Today* **2016**, *21(9)*, 1472–1478.
34. Bordel-Vozmediano, S.; Sabir, S.; Benito-Barca, L.; Weigelin, B.; Pérez-García, V.M. Geometric immunosuppression in CAR T-cell treatment: Insights from mathematical modeling. *Comput. Biol. Med.* **2025**, *194*, 110427.
35. Jain, R.K.; Martin, J.D.; Stylianopoulos, T. The role of mechanical forces in tumor growth and therapy. *Annu. Rev. Biomed. Eng.* **2014**, *16*, 321–346.
36. Santurio, D.S.; Paixão, E.A.; Barros, L.R.; Almeida, R.C.; Fassoni, A.C. Mechanisms of resistance to CAR-T cell immunotherapy: Insights from a mathematical model. *Appl. Math. Model.* **2024**, *125*, 1–15.

 doi:10.20944/preprints202603.0742.v1

37. Polyakov, M. Integration of Machine Learning to Personalise a Mathematical Model of Tumour Dynamics Based on Reaction-Diffusion Equations. In: *2025 7th International Conference on Control Systems, Mathematical Modeling, Automation and Energy Efficiency (SUMMA)*; Lipetsk, Russian Federation, **2025**; pp. 776–779.
38. Brady, R.; Enderling, H. Mathematical models of cancer: when to predict novel therapies, and when not to. *Bull. Math. Biol.* **2019**, *81(10)*, 3722-3731.
39. Cappuccio, A.; Tieri, P.; Castiglione, F. Multiscale modelling in immunology: a review. *Brief. Bioinform.* **2016**, *21*(3), 408–418.
40. Norton, K.A.; Gong, C.; Jamalian, S. et al. Multiscale agent-based and hybrid modeling of the tumor immune microenvironment. *Processes* **2019**, *7(1)*, 37.
41. Barrera-León, A.S.; Rodríguez-Quiñones, L.; De Mendoza, A.M. Impact of mild hyperthermia on tumor-immune dynamics explored through mathematical modeling. *Sci. Rep.* **2025**, *15*, 45467.
42. Aderyani, S.R.; Saadati, R.; Aderyani, F.R. et al. Mathematical modeling of tumor-immune dynamics: stability, control, and synchronization via fractional calculus and numerical optimization. *Sci. Rep.* **2025**, *15*, 29094.
43. Liu, H.; Noguera-Ortega, E.; Dong, X. et al. A tumor-on-a-chip for in vitro study of CAR-T cell immunotherapy in solid tumors. *Nat. Biotechnol.* **2025**.
44. Vishwanath, K.; Choi, H.; Gupta, M. et al. Modeling tumor dynamics and predicting response to therapies in a murine pancreatic cancer model. *npj Syst. Biol. Appl.* **2025**, *11*, 123.
45. Keller, E.F.; Segel, L.A. Model for Chemotaxis. *J. Theor. Biol.* **1971**, *30(2)*, 225–234.
46. Owens, K.; Rahman, A.; Bozic, I. Spatiotemporal dynamics of tumor–CAR T-cell interaction following local administration in solid cancers. *PLoS Comput. Biol.* **2025**, *21(6)*, e1013117.
47. Bogle, G.; Dunbar, P.R. Simulating T cell motility in the lymph node paracortex with a packed lattice geometry. *Immunol. Cell Biol.* **2008**, *86(8)*, 676–687.
48. You, R.; Artichoker, J.; Fries, A.; et al. Active surveillance characterizes human intratumoral T cell exhaustion. *J. Clin. Invest.* **2021**, *131(18)*, e144353.
49. Fallahi-Sichani, M.; Kirschner, D.E.; Linderman, J.J. NF-kB signaling dynamics play a key role in infection control in tuberculosis. *Front. Physiol.* **2012**, *3*, 170.
50. DiLeo, M.V.; Kellum, J.A.; Federspiel, W.J. A simple mathematical model of cytokine capture using a hemoadsorption device. *Ann. Biomed. Eng.* **2009**, *37*(1), 222–229.
51. Hendrata, M.; Sudiono, J. Multiscale modeling of tumor response to vascular endothelial growth factor (VEGF) inhibitor. *In Silico Biol.* **2021**, *14(3-4)*, 71–88.
52. Lam, S.F.; Shirure, V.S.; Chu, Y.E.; Soetikno, A.G.; George, S.C. Microfluidic device to attain high spatial and temporal control of oxygen. *PLOS ONE* **2018**, *13*(12), e0209574.
53. Szafrańska-Łęczycka, M.; Szymańska, Z.; Piotrowska, M.J.; Bodnar, M.; Foryś, U. CAR-T cell therapy for glioblastoma: insight from mathematical modeling. *Front. Immunol.* **2025**, *16*, 1563829.
54. Wigmore, S.J.; Fearon, K.C.H.; Maingay, J.P.; Lai, P.B.; Ross, J.A. Interleukin-8 can mediate acute-phase protein production by isolated human hepatocytes. *Am. J. Physiol.* **1997**, *273(4)*, E720–E726.
55. Kuribayashi, T. Elimination half-lives of interleukin-6 and cytokine-induced neutrophil chemoattractant-1 synthesized in response to inflammatory stimulation in rats. *Lab Anim Res* **2018**, *34*(2), 80–83.
56. Tamm, M.; Bihl, M.; Eickelberg, O.; Stulz, P.; Perruchoud, A.P.; Roth, M. Hypoxia-induced interleukin-6 and interleukin-8 production is mediated by platelet-activating factor and platelet-derived growth factor in primary human lung cells. *Am J Respir Cell Mol Biol* **1998**, *19*(4), 653–661.
57. Mahlbacher, G.; Curtis, L.T.; Lowengrub, J.; Frieboes, H.B. Mathematical modeling of tumor-associated macrophage interactions with the cancer microenvironment. *J Immunother Cancer* **2018**, *6*(1), 10.
58. Huang, A.C.; Orlowski, R.J.; Xu, X.; et al. A single dose of neoadjuvant PD-1 blockade predicts clinical outcomes in resectable melanoma. *Nat Med* **2019**, *25*(3), 454–461.
59. Lai, N.; Farman, A.; Byrne, H.M. The impact of T-cell exhaustion dynamics on tumour–immune interactions and tumour growth. *Bull. Math. Biol.* **2025**, *87(5)*, 61.
60. Oke, S.I.; Matadi, M.B.; Xulu, S.S. Optimal Control Analysis of a Mathematical Model for Breast Cancer. *Math. Comput. Appl.* **2018**, *23*, 21.
61. Gunnarsson, E.B.; Foo, J.; Leder, K. Statistical inference of the rates of cell proliferation and phenotypic switching in cancer. *J. Theor. Biol.* **2023**, *568*, 111497.
62. Zhu, X.; Chen, J.; Li, W.; Xu, Y.; Shan, J.; Hong, J.; Zhao, Y.; Xu, H.; Ma, J.; Shen, J.; Qian, C. Hypoxia-Responsive CAR-T Cells Exhibit Reduced Exhaustion and Enhanced Efficacy in Solid Tumors. *Cancer Res.* **2024**, *84*(1), 84–100.

 doi:10.20944/preprints202603.0742.v1

63. Dharani, S.; Cho, H.; Postigo Fernandez, J.; Juillerat, A.; Valton, J.; Duchateau, P.; Poirot, L.; Das, S. TALEN-edited allogeneic inducible dual CAR T cells enable effective targeting of solid tumors while mitigating off-tumor toxicity. *Mol. Ther.* **2024**, *32*(11), 3915–3931.
64. Hu, X.; Ge, C.; Huang, C.; He, D.; Yao, X.; Cheng, J.; Guo, J.; Li, K.; Ye, Y.; Li, L.; Xia, J.; Li, T.; Yao, H. Enhanced homing and efficacy of HER2-CAR T cells via CXCR5/CCR6 co-expression for HER2-positive NSCLC. *J. Transl. Med.* **2025**, *23*(1), 863.
65. Erler, P.; Kurcon, T.; Cho, H.; Skinner, J.; Dixon, C.; Grudman, S.; Rozlan, S.; Dessez, E.; Mumford, B.; Jo, S.; Boyne, A.; Juillerat, A.; Duchateau, P.; Poirot, L.; Aranda-Orgilles, B. Multi-armored allogeneic MUC1 CAR T cells enhance efficacy and safety in triple-negative breast cancer. *Sci. Adv.* **2024**, *10*(35), eadn9857.
66. Conte, M.; Xella, A.; Woodall, R.T.; Cassady, K.A.; Branciamore, S.; Brown, C.E.; Rockne, R.C. CAR T-cell and oncolytic virus dynamics and determinants of combination therapy success for glioblastoma. *Math. Biosci.* **2025**, *389*, 109531.